AFRL-RQ-WP-TR-2014-0210

ULTRAVIOLET RAYLEIGH SCATTER IMAGING FOR SPATIAL TEMPERATURE PROFILES IN ATMOSPHERIC MICRODISCHARGES

Steven F. Adams

Electrical Systems Branch
Power and Control Division

James E. Caplinger

UES, Inc.

SEPTEMBER 2014
Interim Report

STINFO COPY

AIR FORCE RESEARCH LABORATORY
AEROSPACE SYSTEMS DIRECTORATE
WRIGHT-PATTERSON AIR FORCE BASE, OH 45433-7541
AIR FORCE MATERIEL COMMAND
UNITED STATES AIR FORCE

NOTICE AND SIGNATURE PAGE

*//Signature//   //Signature//
STEVEN F. ADAMS   GREG FRONISTA
Program Manager   Branch Chief
Electrical Systems Branch   Electrical Systems Branch
Power and Control Division   Power and Control Division

//Signature//
JOHN G. NAIRUS, Chief Engineer
Power and Control Division
Aerospace Systems Directorate

1. REPORT DATE (DD-MM-YY) September 2014	2. REPORT TYPE Interim	3. DATES COVERED (From - To) 21 December 2012 – 21 September 2014

4. TITLE AND SUBTITLE ULTRAVIOLET RAYLEIGH SCATTER IMAGING FOR SPATIAL TEMPERATURE PROFILES IN ATMOSPHERIC MICRODISCHARGES	5a. CONTRACT NUMBER In-house
	5b. GRANT NUMBER
	5c. PROGRAM ELEMENT NUMBER 61102F
6. AUTHOR(S) Steven F. Adams (AFRL/RQQE) James E. Caplinger (UES, Inc.)	5d. PROJECT NUMBER 2301
	5e. TASK NUMBER
	5f. WORK UNIT NUMBER Q126

7. PERFORMING ORGANIZATION NAME(S) AND ADDRESS(ES) Electrical Systems Branch (AFRL/RQQE) Power and Control Division Air Force Research Laboratory, Aerospace Systems Directorate Wright-Patterson Air Force Base, OH 45433-7541 Air Force Materiel Command, United States Air Force	UES, Inc. 4401 Dayton-Xenia Road Dayton, OH 45432	8. PERFORMING ORGANIZATION REPORT NUMBER AFRL-RQ-WP-TR-2014-0210

9. SPONSORING/MONITORING AGENCY NAME(S) AND ADDRESS(ES) Air Force Research Laboratory Aerospace Systems Directorate Wright-Patterson Air Force Base, OH 45433-7541 Air Force Materiel Command United States Air Force	10. SPONSORING/MONITORING AGENCY ACRONYM(S) AFRL/RQQE
	11. SPONSORING/MONITORING AGENCY REPORT NUMBER(S) AFRL-RQ-WP-TR-2014-0210

12. DISTRIBUTION/AVAILABILITY STATEMENT
Approved for public release; distribution unlimited.

13. SUPPLEMENTARY NOTES
PA Case Number: 88ABW-2014-4411; Clearance Date: 18 Sep 2014.

14. ABSTRACT
Spatially resolved temperature measurements within a microdischarge in atmospheric pressure air have been conducted using Rayleigh scattering of a pulsed ultraviolet laser. Scattering intensity images were used to generate a radial profile of translational temperature, with the analysis based on the ideal gas inverse relationship of temperature and gas density. Rayleigh scattering results were compared to standard optical emission spectral analyses of $N_2(C^3\Pi_u \rightarrow B^3\Pi_g)$ bands, where the calculated rotational temperatures from emission were in reasonable agreement with the Rayleigh translational temperature profiles.

15. SUBJECT TERMS
ultraviolet laser, Rayleigh scatter microdischarge, translational temperature, temperature mapping, optical emission

16. SECURITY CLASSIFICATION OF:			17. LIMITATION OF ABSTRACT: SAR	18. NUMBER OF PAGES 60	19a. NAME OF RESPONSIBLE PERSON (Monitor) Steven F. Adams
a. REPORT Unclassified	b. ABSTRACT Unclassified	c. THIS PAGE Unclassified			19b. TELEPHONE NUMBER (Include Area Code) N/A

TABLE OF CONTENTS

LIST OF FIGURES

List of Tables

ACKNOWLEDGMENTS

1   SUMMARY

Spatially resolved temperature measurements within a microdischarge in atmospheric pressure air have been conducted using Rayleigh scattering of a pulsed ultraviolet laser. Scattering intensity images were used to generate a radial profile of translational temperature, with the analysis based on the ideal gas inverse relationship of temperature and gas density. Rayleigh scattering results were compared to standard optical emission spectral analyses of specific $N_2(C^3\Pi_u \rightarrow B^3\Pi_g)$ bands, where the calculated rotational temperatures from emission were in reasonable agreement with the Rayleigh translational temperature profiles.

2   INTRODUCTION

A great interest has emerged over the past decade in atmospheric pressure plasma discharges due to the lower costs and simplified operation in comparison with low pressure plasma processing as well as unique biomedical and environmental applications. These atmospheric discharges also offer the advantage of avoiding the use of an elaborate vacuum system, decreasing the time of sample preparation, simplifying the transfer of samples and allowing a more continuous processing or production design [1] [2] [3] [4]. Additional benefits are gained with atmospheric pressure non-thermal plasma, which is characterized by a nonequilibrium distribution of energy within the various particles and degrees of freedom in the plasma. A nonthermal plasma is described, not by a single temperature, but by a set of temperatures including electron temperature (T_e) relating to the translational energy distribution of the electrons, as well as several molecular temperatures, T_{trans} , T_{vib}, and T_{rot} relating to the translational, vibrational and rotational energies of the molecule. Typically this temperature set in a nonthermal plasma will have the characteristic of $T_e >> T_{vib} > T_{trans} = T_{rot}$ [5]. An important advantage of this nonequilibrium environment is that a sample in contact with the nonthermal plasma can be exposed to the active species, allowing favorable processing to occur without absorbing excessive heat that may cause damage or unfavorable reactions [6].

Sustaining a nonthermal atmospheric plasma can be achieved with a so-called "normal glow discharge," which under atmospheric pressure must be scaled down to a characteristic electrode gap separation of less than 1 mm [1]. These small dimension atmospheric normal glow discharges are often termed as microplasmas or microdischarges. Such microdischarges in air are nonthermal plasmas with translational gas temperatures ranging from several hundred to over 1,000 K. The applications may be somewhat limited by the small size of the air microdischarge, but interest is growing as these devices become more stable and large areas are achieved through designs of multiple microdischarge sources or microdischarge arrays.

Accurate measurement of the temperature set associated with an air microdischarge is critical to the fundamental understanding of the kinetics within the plasma source, optimization of the source design, and the prediction of reactions via plasma radicals [7]. The gas temperature of laboratory microplasma jets have been measured previously with a thermocouple downstream of the jet [8], but probing the active microplasma region with a thermocouple would likely influence the fluid, chemical, or electrical characteristics of the system. Noninvasive methods of measuring microplasma temperature, such as remote optical sensing, are clearly more valuable as experimental diagnostics [9] [10].

This work focuses on two techniques to noninvasively measure the rotational and translational temperatures respectively of an atmospheric microdischarge, namely the widely published technique of optical emission spectroscopy of the N_2 second positive system [11] [12] and a more novel technique introduced here of imaging the Rayleigh scatter [13] from an ultraviolet pulsed laser.

There are a variety of optical scattering mechanisms which are commonly analyzed to measure plasma parameters, with the most routinely used for plasma diagnostics being Thomson, Raman and Rayleigh scattering. Thomson scattering refers to scattering off of electrons or, in the collective regime, ions as well. The Thomson scattering spectrum is asymmetric, shifted about the incident wavelength and is routinely modeled to extract both the electron temperature and

2

electron density. In contrast, Raman scattering refers to inelastic scattering from the discrete rotational and vibrational structure of gas molecules. Like Thomson scattering, Raman scattering spectra are also asymmetric and shifted about the incident wavelength. The rotational and vibrational energies of the scattering molecule can be modeled to a Boltzmann distribution and the corresponding Raman spectral structure fit to experimental Raman scattering spectra in order to extract both rotational and vibrational temperatures of a particular species. Rayleigh scattering is a broad term for any elastic light scattering in which the incident wavelength is much larger than the scattering particle (scattering in which the incident wavelength is smaller than the scattering particle is known as Mie scattering). In the case of a gas discharge, Rayleigh scattering refers to all elastic scattering from gas particles. There are two methods of determining temperature from Rayleigh scattering. The line shape of the Rayleigh scattering spectrum can be fit to extract temperature based on temperature and pressure dependent broadening, or, as is the case in this work, the temperature can be extracted by relating the Rayleigh scatter intensity to gas density and using the ideal gas law at a constant pressure to isolate the translational gas temperature. In the second case, the technique known as filtered Rayleigh scattering (FRS) is commonly used in order to strongly suppress stray light scatter and isolate Rayleigh scatter. In many cases Rayleigh, Raman and Thomson scattering are all superimposed in a spectral region surrounding the incident wavelength. Thus, to extract Thomson, Rayleigh and Raman scattering information, high resolution filtering is often necessary to remove the elastic Rayleigh peak centered at the incident wavelength along with stray scattered light at the same wavelength. This is generally accomplished using multiple spectrometer gratings and a mask to filter the incident wavelength. If the electron densities are sufficiently high relative to gas densities, Thomson scattering will dominate. While at higher gas densities, as is the case at atmospheric pressure, Rayleigh and Raman scattering are dominant. The regime at which each diagnostic technique is applicable is highly dependent upon operating pressure and ionization. However, theses regimes can be extended by the use of high-resolution spectrometers and specialized filtering.

Typically, it is difficult to separate stray laser light from Rayleigh scatter, however, by imaging the laser waist, the majority of stray light can be spatially filtered to isolate the Rayleigh scatter. This technique is also advantageous when compared to similar gas temperature measurement techniques, such as filtered Rayleigh scattering and rotational Raman scattering, as no spectrometer or elaborate spectral filtering is required.

The major constituents of air, specifically N_2 and O_2, are not easily accessible to many common optical diagnostic techniques since they are homo-nuclear diatomic molecules with zero dipole moment. In nitrogen containing plasmas, optical emission spectroscopy (OES) is commonly applied as a non-invasive, remote temperature measurement technique. The technique often involves the analysis of the $N_2(C^3\Pi_u \rightarrow B^3\Pi_g)$ emission bands (the so-called second positive system) where a rotational temperature is usually assigned from a contour analysis of the emission spectrum. Contour fitting is required due to the congestion and complicated nature of the band which results in an unresolved rotational spectrum [12]. The rotational temperatures determined from $N_2(C^3\Pi_u \rightarrow B^3\Pi_g)$ emission have been generally deemed acceptable representations of the $N_2(X^1\Pi_g)$ ground state gas temperature [11], but it should be noted these analyses depend strongly on an assumption that the rotational distribution of the $N_2(C^3\Pi_u)$ state is Boltzmann, and identical to that of the $N_2(X^1\Pi_g)$ ground state.   Further analysis of the various vibrational bands within the $N_2(C^3\Pi_u \rightarrow B^3\Pi_g)$ spectrum often results in the determination of a vibration temperature associated with the discharge [14], which is also subject

3

to the assumption that the internal energy distribution within the $N_2(C^3\Pi_u)$ and $N_2(X^1\Pi_g)$ states are identical. Although this assumption is commonly invoked, conclusive evidence that supports or refutes that $N_2(C^3\Pi_u)$ and $N_2(X^1\Pi_g)$ have equivalent rotational energy distributions has not been published to date.

In this experiment, the OES technique described above for microdischarge temperature measurement is compared to the technique of probing an air microdischarge with ultraviolet laser radiation at 266 nm, collecting the Rayleigh scatter image and determining the translational temperature, or T_{trans}. With the majority of Rayleigh scattering target molecules in the air microdischarge being of the $N_2(X^1\Pi_g)$ state, there exists an opportunity to investigate the validity of the common assumption that T_{trans} of the $N_2(X^1\Pi_g)$ state, measured here with Rayleigh scatter imaging, is equal to T_{rot} of the $N_2(C^3\Pi_u)$ state, measured here in OES. Additionally, two-dimensional, radially resolved gas temperature maps using laser Rayleigh scattering are presented with a relatively high spatial resolution of 20 µm.

3   THEORY

3.1   Non-Thermal Microdischarge Plasmas

A plasma, as originally defined by Langmuir in 1926, described a region of a gas discharge in which there were equal amounts of electrons and ions present [15] [16]. Today, plasmas have a much broader definition; any group of particles whose behavior is dominated by long-range coulomb interactions. Within this wide definition are classifications based on the amount of ionization, effect of collisions, overall energy, and whether the plasma is thermal [15]. The specific focus of this work is analyses of the so-called nonthermal microdischarge plasmas which operate in the normal glow mode. Normal glow discharges are often termed plasmas because their charged particles do exhibit strong long-range Coulomb interactions. However, due to their high neutral density and subsequent low ionization, many working in the field of high density and high temperature plasma physics would argue they don't qualify as plasmas. Often additional descriptors are used for these normal glow discharges, such as "weakly ionized gases" or "low temperature plasmas." Regardless of the terminology, these normal glow discharges have unique and useful characteristics and their potential for commercial, medical, and military application grows as our understanding of their behavior expands.

As stated in the introduction, these atmospheric microdischarges are non-thermal because their translational, rotational, vibrational and electron temperatures are not in equilibrium and, in general, for a non-thermal discharge: $T_{Translational} \cong T_{Rotational} \ll T_{Vibrational} \ll T_{Electron}$. We deem these specific devices microdischarges because they are on a scale of less than 1 millimeter, usually dictated by near atmospheric pressure operation and the physics of sustaining a glow discharge under such conditions. Additionally, because this discharge is operated at atmospheric pressure, its behavior deviates somewhat from that of a low pressure, low temperature discharge due to its highly collisional nature.

Normal glow discharges typically operate between 10^{-5} and 10^{-2} amperes of current and have a typical electrical potential drop ranging from approximately 400 to 700 V. The term normal explicitly means that the discharge has a constant current density and constant voltage over a specific electrical current range [12]. As the current exceeds the normal discharge range, the voltage increases and the discharge operates in the abnormal glow mode. In the normal glow mode the voltage drop is generally independent of discharge current for several orders of magnitude, which manifests itself experimentally as a relatively flat section on an I-V curve.

The electrical breakdown process is important in creating a gas discharge. Gas breakdown occurs within an initially neutral gas when an applied voltage is high enough to allow for an electron avalanche to initiate the breakdown of the particular gas, which is known as the Townsend breakdown, and is usually initiated by a cosmic ray for its first ionization [17]. The relationship between breakdown voltage, V_b, and the product of pressure and electrode separation, Pd, is known as Paschen's law. Friedrich Paschen derived the relationship in 1889 based on the two fundamental mechanisms necessary for creating charge carriers and thus sustaining a gas discharge. The first mechanism is ionization caused by energetic electron collisions with neutrals, known as the α process. The second is known as secondary electron emission and occurs when electrons are emitted from the cathode as a result of ion impact, known as the γ process [18]. By understanding these two mechanisms, Paschen was able to derive the following equation,

$$V_b = \frac{B\,Pd}{\ln(Pd) + \ln\left[\frac{A}{\ln(1/\gamma_i + 1)}\right]} \; ,$$

(1)

where A and B are coefficients of the particular gas and are derived from a fit function of Townsends first ionization coefficient, α , P is the pressure, d is the electrode separation and γ_i is the Townsend second ionization coefficient and is defined as $\gamma_i = n_{secondary}/n_i$. This equation may be applied to derive the breakdown thresholds for dc air microdischarges using the empirically determined values for air of A=15 V/(cm·Torr) and B=365 V and a typical value of $\gamma_i = 0.1$. For a 1 mm gap air microdischarge, this gives a breakdown threshold voltage of 4,500 V, and is consistent with data for breakdown in small air gaps [19]. For a gap of 0.75 mm, which is applicable to the experiments in this study, the threshold breakdown voltage is predicted to be 3,540 V, which is a threshold breakdown field of 4,720 V/mm.

Figure 1 below shows the general architecture of a normal glow discharge, including the primary emissive regions of the negative glow and positive column. The brightest and most energetic region is the negative glow. The positive column is characterized by its large volume and uniformity. Because of the emissive dominance of these two regions they are most commonly studied using optical emission spectroscopy, and in fact, emission systems of common gases are named by their prominence in these regions. For example, emission from the $N_2^+(B \rightarrow X)$ transition, with the most prominent band head at 391 nm, is known as the first negative system because it is the most emissive system belonging to the negative glow. The emission from the $N_2(C^3\Pi_u \rightarrow B^3\Pi_g)$ transition, which is analyzed in this work, is termed the second positive system due to its relative prominence in the positive column.
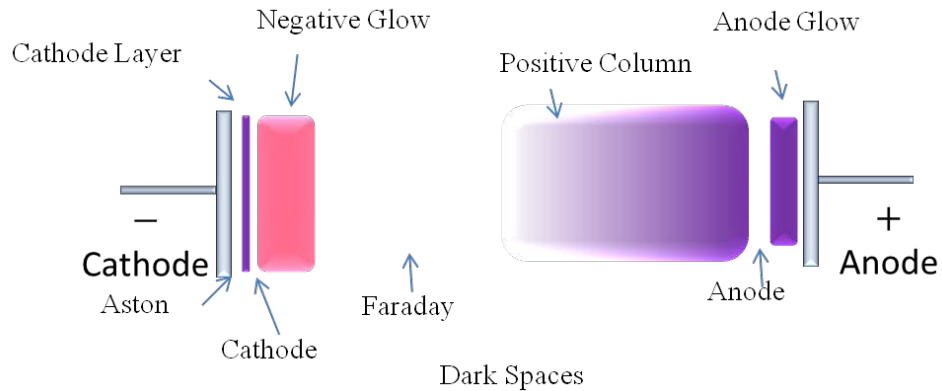
Figure 1: General Glow Discharge Architecture

(Figure 1 shows different regions discussed in literature, based on a figure used by Nasser in 1971 [12].)

3.2   Discharge Power and Gas Temperature

The argument below follows closely from a derivation made by Staack et al. in 2006 [20]. Once an atmospheric air discharge is sustained, two primary mechanisms govern cooling for the discharge, radial cooling caused by surrounding gas and axial cooling through the electrodes. The theory below will show that for relatively large gap microdischarges, the less efficient gas

radial cooling is dominant and gas temperature will rise with discharge current, whereas for short gap microdischarges, electrode axial cooling is dominate and the gas temperature will stay constant along with the current density as the discharge current is increased. Approximating an atmospheric normal glow discharge as a cylindrical heat source, the discharge power can be expressed as [20],

$$\omega_p = IV_{gap} \, , \tag{2}$$

where ω_p is the discharge power, I is the current and V_{gap} is the voltage drop across the electrodes. Here the current may be expressed as $I = \pi R^2 j$, where R is the effective radius and j is the current density, which gives

$$\tag{3}$$
$$\omega_p = \pi R^2 j V_{gap} \, .$$

For an ideal normal glow discharge, the current density j remains constant with changing current, thus the discharge cross sectional area, or πR^2, will be directly proportional to the discharge current. The effective radial cooling rate due to heat transfer with surrounding gas can be expressed as

$$\tag{4}$$
$$q_{radial} = (2\pi R d) h_{radial} \Delta T \, ,$$

where h_{radial} is a heat transfer efficiency term dependent upon gas diffusion and ΔT is the temperature differential between the discharge and the surrounding gas. For this case, the surrounding gas can be treated as a cooling shell and h_{radial} can be written as a function of our effective radius (because the interaction area determines gas diffusion efficiency) as shown below.

$$\tag{5}$$
$$h_{radial} = \frac{k}{\left(R ln(R_\infty/R)\right)}$$

Here k is the conductivity of the gas while R_∞ is an outside boundary defined by the radius at which the temperature gradient approaches zero. Setting the heat transfer rate equal to the discharge power and substituting in h_{radial} we can show that

$$\pi R^2 j V_{gap} = (2\pi R d) \frac{k}{\left(R ln(R_\infty/R)\right)} \Delta T \, . \tag{6}$$

This simplifies to

$$\pi R^2 j \, V_{gap} = \frac{2\pi d k}{ln(R_\infty/R)} \Delta T \, . \tag{7}$$

Approved for public release; distribution unlimited.

The logarithm in the denominator can be shown to vary slowly with R and thus can be approximated as a constant of unity value [5]. Solving for ΔT and substituting the discharge current back in we find that

$$\Delta T \approx \frac{IV_{gap}}{2\pi dk}.$$

(8)

This result indicates that if radial heat diffusion to the surrounding gas were the cooling method, the temperature would be proportional to the discharge current. For the case of axial cooling through the electrodes, the axial heat transfer efficiency term, h_{axial}, is constant for highly conductive electrodes and does not depend upon the discharge size. It can thereby be shown in a similar manner as above that

$$\Delta T \approx \frac{jV_{gap}}{h_{axial}}.$$

(9)

Thus the gas temperature can only be related to the current density, which as stated before is nominally constant for a normal glow discharge [20].

A microdischarge with a sufficiently small gap loses heat very efficiently through the axial cooling from the electrodes. This short microdischarge may exhibit a flat current-voltage curve which indicates that the current increase is due only to an increased discharge area. For such a sufficiently short microdischarge, the gas temperature would be expected to remain constant with increasing current. Microdischarge cooling is not as efficient for larger gaps, because the conductivity of the gas is much less than that of the metal electrodes. Microdischarges with larger electrode spacing are common in the literature and the current-voltage characteristics have been found to have a small negative differential resistance, dV/dI [20].This is because, with less efficient heat loss, the microdischarge temperature increases with gap length, resulting in growth of conductivity, as well as discharge cross sectional area, with increasing current. Thus, a small negative differential resistance would also indicate that the microdischarge gas temperature should increase somewhat with increasing discharge current. Many atmospheric microdischarges have a slight negative differential resistance characteristic, but are often still considered to be in the class of normal discharges.

3.3   Electronic, Vibrational and Rotational Structure of N_2

The emission observed from an N_2 or atmospheric air plasma contains a wealth of information that can be derived from spectral analysis. From such a spectrum, one can determine relative densities of energetic states or radical species, an estimate of the electron temperature, vibrational temperatures, and most importantly for this work: the rotational temperatures. By understanding the rotational, vibrational and electronic structure of a diatomic molecule, such as molecular nitrogen, one can use the emission model discussed in the following section to derive the rotational temperature from the optical emission of an N_2 plasma.

The wave function and associated energy levels of molecules containing multi-electron atoms are calculated using the Born-Oppenheimer approximation. This approximation decouples the rotational, vibrational and electronic components of the total wave function. Thus the total wave

function is the product of the individual wave functions and the total energy is the sum of the individual energies as shown in equation (3.11).

$$\Psi_{molecule} = \psi_{el}\psi_{vib}\psi_{rot} \tag{10}$$

$$E_{molecule} = E_{el} + E_{vib} + E_{rot} \tag{11}$$

The wave functions are fundamental in calculating the radiative transition probability between two energy states. The resulting energy structure, shown in Figure 2, along with the transition probabilities are the foundation of our optical emission model. In this work, we focus on the ground state of molecular nitrogen, $N_2(X^1\Sigma_g^+)$, as the most populous in an air discharge, as well as the excited states $C^3\Pi_u$ and $B^3\Pi_g$, since these are involved in the second positive system emission bands. The potential energy curves for the $N_2(X^1\Sigma_g^+)$, $N_2(C^3\Pi_u)$, and $N_2(B^3\Pi_g)$ states are shown in the figure below along with a transition diagram representing the electron excitation to the $N_2(C^3\Pi_u)$, state, as well as the $N_2(C^3\Pi_u, v' = 0 \rightarrow B^3\Pi_g, v'' = 2)$ radiative decay. As the figure shows, the energy difference between electronic states is much greater than the vibrational energy spacing, and the rotational structure is finer still.

The prevalent $N_2(C^3\Pi_u \rightarrow B^3\Pi_g)$ emission in an air discharge begins with direct electronic impact of ground state molecular nitrogen, $N_2(X^1\Sigma_g^+)$. It is generally assumed that the vibrational and rotational population distributions of the $N_2(X^1\Sigma_g^+)$ ground state are mapped onto the excited $N_2(C^3\Pi_u)$ molecules. This assumption is due to the rapidity of the direct electron impact $e^- + N_2(X^1\Sigma_g^+) \rightarrow N_2(C^3\Pi_u)$ excitation and the relatively fast relaxation rate of $N_2(C^3\Pi_u)$, by radiation that prohibits collisional redistribution of the vibrational and rotational population [21] [22]. The radiative lifetime of the resulting $C^3\Pi_u$ state has been previously measured to be between 35-40 ns, depending on the values of v'' and v' [23], and has a dominant transition path down to the less energetic $B^3\Pi_g$ state resulting in near-ultraviolet radiation emission. Because this $N_2(C^3\Pi_u \rightarrow B^3\Pi_g)$ emission spectrum is dependent directly upon the population distribution of the $C^3\Pi_u$ state and the $C^3\Pi_u$ state is assumed to be a direct mapping of the $X^1\Sigma_g^+$ state, any vibrational or rotational temperature derived from analysis of the $N_2(C^3\Pi_u \rightarrow B^3\Pi_g)$ emission spectrum is widely considered to be an equivalent measurement of the ground state temperatures [21] [22]. This, along with the strong intensity and spectral accessibility of the $N_2(C^3\Pi_u \rightarrow B^3\Pi_g)$ emission, is why this set of emission bands is so commonly used in air discharge characterization.
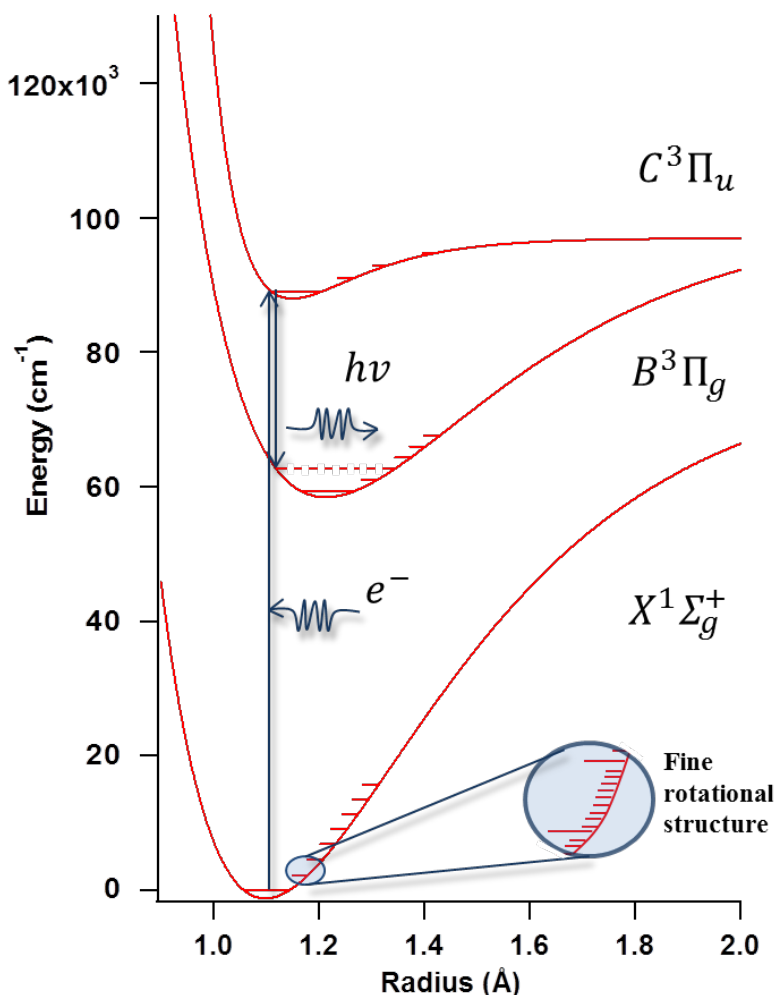
Figure 2: Potential Energy Curves

(The curves in Figure 2 are of $N_2 X^1 \Sigma_g^+$, $N_2 B^3 \Pi_g$, and $N_2 C^3 \Pi_u$. The two step transition shown is given by: 1) $e^- + N_2 X^1 \Sigma_g^+ (v = 0) \rightarrow N_2 C^3 \Pi_u (v = 0)$ and 2) $N_2 C^3 \Pi_u (v = 0) \rightarrow N_2 B^3 \Pi_g (v = 2) + h\nu$ and represents the 'Second Positive System' 0-2 vibrational band head located at approximately 380.71 nm.)

The system of N_2 emission bands which arise from the electronic transition from the excited $C^3 \Pi_u$ to the lower energy $B^3 \Pi_g$ as discussed above is known as the second positive system or SPS. This naming convention was created by Deslandres who first observed and classified the first, second and third positive systems of N_2 as well as the negative groups of the N_2^+ ion in 1885 [21]. The second positive system is so named because it is the *second* most intense system when observing the *positive* column of an ordinary Geissler tube discharge. Table 1 lists wavelengths, relative intensities (reported from 0.9 A, 1.25 Torr N_2 discharge) for prominent vibrational band heads of the SPS [23].

Table 1: Wavelengths and Relative Intensities for Dominant SPS Vibrational Band Heads Commonly Used in Vibrational and Rotational Temperature Analysis [23]

Second Positive System			
λ (nm)	Int.	v'-v''	Δv
337.13	10	0-0	0
333.89	2	1-1	
330.9	2	2-2	
328.53	3	3-3	
357.69	10	0-1	-1
353.67	8	1-2	
350.05	4	2-3	
346.9	0	3-4	
380.49	10	0-2	-2
375.54	10	1-3	
371.05	8	2-4	
367.19	6	3-5	
405.94	8	0-3	-3
399.84	9	1-4	
394.3	8	2-5	
389.46	7	3-6	

3.4 N_2 SPS Model

The $N_2(C^3\Pi_u \to B^3\Pi_g)$ optical emission spectrum can be simulated using tabulated molecular constants and assigning vibrational and rotational temperatures that best fit the experimental data. The line intensity of each radiative transition within the $N_2(C^3\Pi_u \to B^3\Pi_g)$ emission bands can be expressed as [12]

$$I_{n'v'J' \to n''v''J''} = \left(\frac{64\pi^4 c}{3\lambda^4}\right) |\boldsymbol{R}_e|^2 q_{v'v''} S_{j'j''} N_{n'} \exp\left(-\frac{G(v')}{kT_{vib}}\right) \exp\left(-\frac{F_v(J')}{kT_{rot}}\right), \tag{12}$$

where $G(v')$, and $F_v(J')$ are the terms for the respective vibrational, and rotational energies of the $N_2(C^3\Pi_u)$ state, $N_{n'}$ is the total number density of molecules in the $N_2(C^3\Pi_u)$ state, v is the radiation frequency corresponding to the transition energy, c is the speed of light, $\boldsymbol{R}_e$ is the electronic transition moment, $q_{v'v''}$ is the Franck-Condon factor, $S_{J'J''}$ is the Honl-London factor, and k is the Boltzmann constant. The exponential terms at the end of the equation assume a Boltzmann distribution for the vibrational and rotational states in the upper $N_2(C^3\Pi_u)$ state. The Franck-Condon factors indicate the probability of an electronic transition from one vibrational state to another where the highest probability occurs where the vibrational states are most compatible in nuclear positions and momenta. This is because the electronic transition occurs

rapidly compared to the relatively slow by contrast, nuclear and vibrational motion [21]. These Franck-Condon factors are therefore dependent upon the relative geometries of each state's potential energy curve, as shown in Figure 2. Similarly, the Honl-London factors use quantum statistics to determine the branching ratios of radiative transitions in diatomic molecules and thus indicate the probability of transition from one rotational state to another. The combination of the Honl-London and Franck-Condon factors, along with the Boltzmann rotational and vibrational energy distributions in the upper state, give a relative radiative transition probability for each possible transition.

In order to determine temperatures, only a relative fit is needed between the simulated and exponential data. Thus parameters which are constant for all transitions, such as electronic transition moment, the $C^3\Pi_u$ state number density, and the $64\pi^4 c/3$ factor are not required. Therefore, the simulated relative intensity simplifies to

$$
I_{n'v'J' \to n''v''J''} \propto \frac{1}{\lambda^4} q_{v'v''} S_{j'j''} \exp\left(-\frac{G(v')}{kT_{vib}}\right) \exp\left(-\frac{F_v(J')}{kT_{rot}}\right).
$$

(13)

For the $N_2(C^3\Pi_u \to B^3\Pi_g)$ transition studied here, the $q_{v'v''}$ factors were taken from previously tabulated results [24], and are specific to the SPS. The $S_{j'j''}$ factors were calculated from Herzberg's tables [21], for $\Delta\Lambda = 0$ transitions, as is appropriate for the SPS $\Pi \to \Pi$ transition.

For direct comparison with experimental spectra for a given vibrational band, the collection of intensity peak values from equation (13) at their respective wavelengths were calculated for rotational levels from $J = 0$ to 50 for both the $C^3\Pi_u$ and the $B^3\Pi_g$. Because of the fine structure and overlapping nature of the SPS and the instrumental limits of the spectrometer, the rotational structure of the emission cannot be easily resolved and thus a contour fit is most viable. To match the line shape or broadening of each rotational line we convolved the calculated spectra with line shape functions matching the experimental broadening, which in this experiment, was primarily due to the spectrometer line shape. For our model, a pseudo-Voigt line shape was used. A Voigt line shape takes into account both the Lorenztian distribution resulting from the spectrometer slit as well as the Gaussian distribution from Doppler broadening. The pseudo-Voigt is a computationally efficient approximation of the Voigt line shape. Finally, an iterative least-square fitting algorithm was used to find the best fit rotational temperature by allowing the rotational and vibrational temperatures to be the only dynamic parameters.

3.5   Rayleigh Scattering Theory

This work is focused on analyzing Rayleigh scattering from a laser beam passing transversely through an air microdischarge with the intent of extracting spatially resolved gas temperatures. In order to do so, a general understanding of Rayleigh scattering cross sections and total laser Rayleigh scatter intensity is required, along with the relationship between the thermodynamic state of the scattering volume and the corresponding scatter intensity. This section describes the origins of Rayleigh scattering theory and outlines the relationships necessary to complete the temperature analysis from the laser scatter portion of the study.

Rayleigh scattering refers to elastic photon scattering in which the wavelength of incident scattered light is much larger than the scattering particle itself, which is true for visible and near

Approved for public release; distribution unlimited.

visible light scattering from air molecules [13]. Alternatively, scattering in which the scattering particle is larger than the incident wavelength is known as Mie scattering. Since Rayleigh scattering is elastic photon scattering, this indicates that the scattered photon energy (and wavelength) is the same as the incident photon energy (and wavelength), leaving the particle in the same state as before the scattering event. In practice, however, the collection of scattered light often also includes at least some inelastic vibrational and rotational Raman scattering, which is shifted in wavelength, but, in general, much weaker than the Rayleigh scattering. From a historical perspective, Lord Rayleigh's theory for light scattering from gases in 1871 was originally developed to explain the observed blue color of the sky. In that context, he showed empirically that the total scattering cross section per molecule is proportional to $1/\lambda^4$. The $1/\lambda^4$ factor implies a higher scattering efficiency for shorter wavelength light, or bluer light, and a lower efficiency for longer wavelength light, or redder light. Rayleigh explained that the bluer light within the Sun's spectrum was more efficiently scattered, leaving our sky a pale blue as viewed from Earth and conversely giving the Sun a yellowish hue. This famous explanation is now referred to as Rayleigh's law. Rayleigh's law predicted that sunlight observed from indirect angles after scattering from atmospheric molecules would contain much more blue because a greater portion of blue light is scattered from the indirect solar rays [25]. Similarly, a sunset near the horizon appears reddish because the direct solar rays travel further through the atmosphere and interact with more scattering molecules before arriving at the observer, thus more blue light is scattered away from the sunlight through a line-integrated attenuation, leaving the spectrum more red than blue. This $1/\lambda^4$ factor in Rayleigh's Law can also be applied to the advantage of an experimenter who is striving to maximize their scatter signal, where using a bluer source of radiation would generally increase the scatter intensity. However this also means greater overall attenuation of the incident beam, therefore, the same advantages may not apply to long range sensing applications where attenuation is a concern.

The most general result describing the intensity of Rayleigh scatter is derived by approximating all scattering particles as spherically symmetric, where the scattered radiation is sufficiently described by simple dipole radiation. The scattered radiation is therefore given by

$$I_s = \frac{\pi^2 c p^2 \sin^2 \varphi}{2\varepsilon_0 \lambda^4 r^2},$$

(14)

where c is the speed of light, p is the dipole moment, ε_0 is the vacuum permittivity, λ is the incident wavelength, r is the observation distance, and φ is the angle of observation from the incident radiation propagation vector as defined by the scattering coordinate system defined by Figure 3. It can be seen that due to the spherically symmetric nature of the particle, the scatter intensity has neither radial angular dependence nor polarization dependence. This is a very good approximation of Rayleigh scattering for atomic gases, such as helium and argon.
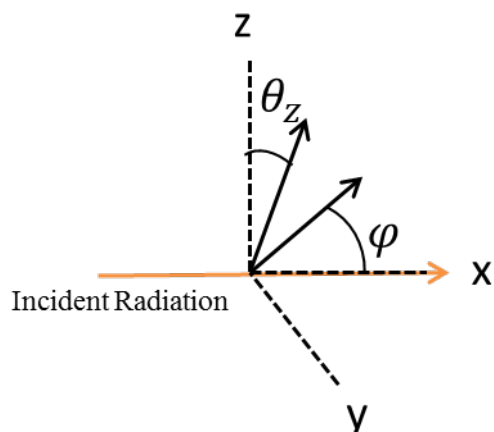
Figure 3: Scattering coordinate system

However, for molecules which are not spherically symmetric, a more rigorous description of Rayleigh scattering is necessary in order to account for the anisotropic nature. Here, a derivation of Rayleigh scatter cross sections for diatomic molecules will be presented, as this work was conducted in atmospheric air containing largely the diatomic molecules, N_2 and O_2, and using a horizontally polarized laser.

For a laser propagating in the horizontal x direction, linearly polarized in the horizontal y direction and the z direction being vertically upward as shown in Figure 4, we consider scatter from a randomly oriented diatomic molecule with an induced polarization, $\vec{p}$. From this oscillation induced dipole, radiation may be distributed throughout the full angular geometry, however, for this theoretical derivation we consider only radiation that is observed at right angles to the laser propagation, i.e. the y-z plane. This simplified configuration makes practical sense, as Rayleigh scattering from diatomic molecules is known to have the same φ dependence as the spherically symmetric scattering described by equation (14) and thus the observed scatter will be at a maximum in the y-z plane. The scattered radiation propagating in the y-z plane has an associated oscillating field, $\overrightarrow{E_s}$, orthogonal to the propagation vector. We can determine convenient components of $\overrightarrow{E_s}$ by defining $\hat{H}$ as the horizontal unit vector along the x axis and $\hat{V}$ the vertical unit vector, which is not entirely vertical, as the name suggests, but lies in the y-z plane, perpendicular to both $\hat{H}$ and the scattered propagation. Our scatter geometry is illustrated in Figure 4 below.
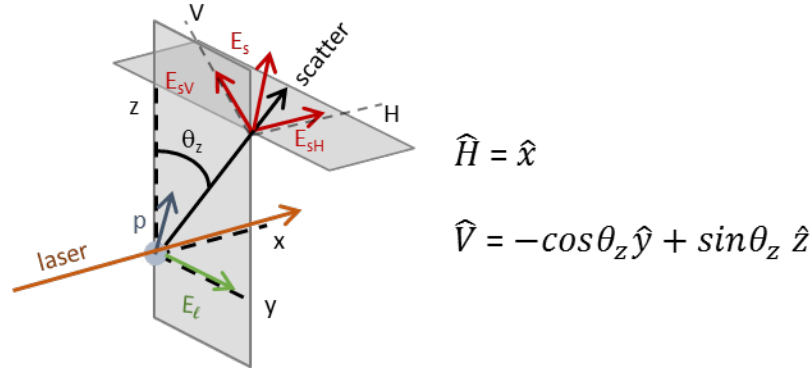
Figure 4: Scatter geometry for horizontally polarized laser scattering off of a diatomic molecule, restricted to the y-z plane.

$$\hat{H} = \hat{x}$$

$$\hat{V} = -\cos\theta_z \hat{y} + \sin\theta_z \hat{z}$$

The scattered electric field, $\vec{E_s}$, is approximated as the response of a dipole antenna and depolarized into separate E_{sH} and E_{sV} components as in the following equations

$$E_{sH} = \frac{\pi \left| \vec{p} \cdot \hat{H} \right|}{\varepsilon_o \lambda^2 r} \tag{15}$$

$$E_{sV} = \frac{\pi \left| \vec{p} \cdot \hat{V} \right|}{\varepsilon_o \lambda^2 r} \tag{16}$$

where $\vec{p}$ is the polarization of the molecule, which is randomly oriented and may have any combination of x, y and z components. From our definitions of $\hat{H}$ and $\hat{V}$ it can easily be seen that

$$\vec{p} \cdot \hat{H} = p_x \tag{17}$$

$$\vec{p} \cdot \hat{V} = -p_y \cos\theta_z + p_z \sin\theta_z. \tag{18}$$

The intensity of scattered dipole radiation is defined as

$$I_s = \frac{\varepsilon_o c \left| \vec{E_s} \right|^2}{2} . \tag{19}$$

Thus, the H and V components of this intensity are given as

$$I_{sH} = \frac{\pi^2 c}{2\varepsilon_o \lambda^4 r^2} [p_x]^2 \qquad (20)$$

and

$$I_{sV} = \frac{\pi^2 c}{2\varepsilon_o \lambda^4 r^2} [p_z sin\theta_z - p_y cos\theta_z]^2 \qquad (21)$$

$$= \frac{\pi^2 c}{2\varepsilon_o \lambda^4 r^2} [p_y{}^2 cos^2\theta_z - p_y p_z cos\theta_z sin\theta_z - p_z{}^2 sin^2\theta_z] .$$

The components of the polarization of the molecule, $\vec{p}$, are given by the symmetric polarizability tensor α_{ij}, as [13]

$$p_x = \alpha_{xx} E_{lx} + \alpha_{xy} E_{ly} + \alpha_{xz} E_{lz}$$

$$p_y = \alpha_{yx} E_{lx} + \alpha_{yy} E_{ly} + \alpha_{yz} E_{lz}$$

$$p_z = \alpha_{zx} E_{lx} + \alpha_{zy} E_{ly} + \alpha_{zz} E_{lz} \qquad (22)$$

where E_{li} is the electric field of the laser with linear polarization in the $\hat{i}$ direction. However, in our experiment, the laser is propagating in the x direction and is linearly polarized in the y direction, so $E_l = E_{ly}$ and the tensor representing the horizontally polarized laser used in our laboratory simplifies to

$$p_x = \alpha_{xy} E_l$$

$$p_y = \alpha_{yy} E_l$$

$$p_z = \alpha_{zy} E_l. \qquad (23)$$

Substituting these factors, as well as the laser intensity given by $I_{laser} = \varepsilon_o c E_l^2 / 2$, our scatter intensity components become

$$I_{sH} = \frac{\pi^2 I_{laser}}{\varepsilon_o{}^2 \lambda^4 r^2} \alpha_{xy}{}^2 \qquad (24)$$

$$I_{sV} = \frac{\pi^2 I_{laser}}{\varepsilon_o{}^2 \lambda^4 r^2} [\alpha_{yy}{}^2 cos^2\theta_z - \alpha_{yy}\alpha_{zy} cos\theta_z sin\theta_z - \alpha_{zy}{}^2 sin^2\theta_z]. \qquad (25)$$

To further define the polarizability tensor for air molecules, a polarizability ellipsoid is introduced [13] with a mean polarizability, a, and the anisotropy, γ given by the following equations

$$a^2 = \frac{1}{9}\left(\alpha_{\underline{xx}} + \alpha_{\underline{yy}} + \alpha_{\underline{zz}}\right)^2 \tag{26}$$

$$\gamma^2 = \frac{1}{2}\left\{\left(\alpha_{\underline{xx}} - \alpha_{\underline{yy}}\right)^2 + \left(\alpha_{\underline{yy}} - \alpha_{zz}\right)^2 + \left(\alpha_{zz} - \alpha_{\underline{xx}}\right)^2 \right. \\ \left. + 6\left(\alpha_{\underline{xy}}^2 + \alpha_{\underline{yz}}^2 + \alpha_{\underline{zx}}^2\right)^2\right\}. \tag{27}$$

In the case of a diatomic molecule with cylindrical symmetry, the polarizabilities in the y and z directions are equal, so that $\alpha_{yy} = \alpha_{zz}$. This means that a and γ become

$$a^2 = \frac{1}{9}\left(\alpha_{\underline{xx}} + 2\alpha_{\underline{yy}}\right)^2 \tag{28}$$

$$\gamma^2 = \left(\alpha_{\underline{xx}} - \alpha_{\underline{yy}}\right)^2. \tag{29}$$

If we now recognize the molecule as freely rotating, it is necessary to average over all the orientations taken by the diatomic molecule with respect to the laser electric field. Long [26] has conducted the space-averaged calculations of the squares of the polarizability tensor components with the results

$$\overline{\alpha_{\underline{xx}}^2} = \overline{\alpha_{yy}^2} = \overline{\alpha_{\underline{zz}}^2} = \frac{45a^2 + 4\gamma^2}{45} \tag{30}$$

$$\overline{\alpha_{\underline{xy}}^2} = \overline{\alpha_{\underline{xz}}^2} = \overline{\alpha_{\underline{yx}}^2} = \overline{\alpha_{\underline{yz}}^2} = \overline{\alpha_{\underline{zx}}^2} = \overline{\alpha_{\underline{zy}}^2} = \frac{3\gamma^2}{45} \tag{31}$$

while all terms which involve any subscript once only, such as $\alpha_{yy}\alpha_{zy}$, were shown by Long to be zero. This allows the scatter intensity per molecule as observed in the y-z plane to be expressed in terms of a and γ as

$$I_{sH} = \frac{\pi^2}{\varepsilon_o^2\lambda^4 r^2}\frac{I_{laser}}{45}\frac{3\gamma^2}{45} \tag{32}$$

and

Approved for public release; distribution unlimited.

$$I_{sV} = \frac{\pi^2 \, I_{laser}}{\varepsilon_o^2 \lambda^4 r^2} \left[\frac{45a^2 + 4\gamma^2}{45} \cos^2 \theta_z + \frac{3\gamma^2}{45} \sin^2 \theta_z \right]. \tag{33}$$

The I_{sV} component can be further reduced as

$$I_{sV} = \frac{\pi^2 \, I_{laser}}{\varepsilon_o^2 \lambda^4 r^2} \left[\frac{45a^2 + 4\gamma^2}{45} \cos^2 \theta_z + \frac{3\gamma^2}{45} (1 - \cos^2 \theta_z) \right]$$

or

$$I_{sV} = \frac{\pi^2 \, I_{laser}}{\varepsilon_o^2 \lambda^4 r^2} \left[\frac{45a^2 + \gamma^2}{45} \cos^2 \theta_z - \frac{3\gamma^2}{45} \right]. \tag{34}$$

From the equations above we can see that only the vertically polarized light has a dependence on the angle of observation. Now considering a randomly oriented sample of molecules where N is the molecular number density and V is the observed volume, and combining the two polarizations, the total scatter intensity is

$$I_{scatter} = \frac{NV\pi^2 \, I_{laser}}{\varepsilon_o^2 \lambda^4 r^2} \left[\left(\frac{45a^2 + \gamma^2}{45} \right) \cos^2 \theta_z + \frac{6\gamma^2}{45} \right]. \tag{35}$$

By treating all air molecules as having an effective mean polarizability and anisotropy we can accurately prescribe the above equation for our case. Miles [13] provides effective values in air of $a = 0.0336$ and $\gamma = 0.0173$ for laser light at 266 nm, as is the case for this work. Thus, our final expression for Rayleigh scatter intensity from atmospheric air observed in a plane perpendicular to the propagation of a 266 nm laser is

$$I_{scatter} = \frac{NV\pi^2 \, I_{laser}}{\varepsilon_o^2 \lambda^4 r^2} [(1.176 \times 10^{-3}) \cos^2 \theta_z + 3.99 \times 10^{-5}]. \tag{36}$$

Two important implications concerning the experimental set up can be made immediately from the above expression. First, it is obvious that a maximum scatter signal is obtained for this horizontally polarized laser when observing at an angle of $\theta_z = 0$, which is when the scattered light is collected in the vertical direction. The theoretical ratio of the vertical to horizontal scatter signals collected orthogonal to the laser propagation is approximate 29×. Also, since this higher intensity angular dependent portion of $I_{scatter}$ originated from the I_{sV} component, it has only vertical polarization. This indicates that experimental techniques such as filtering out or background subtracting the horizontally polarized scattered light could assist in eliminating stray laser light and isolating the signal of the strongest Rayleigh scatter term. Second, as discussed previously, the incident wavelength dependence greatly favors experiments using lower wavelength ultraviolet lasers, as long as the attenuation of the laser is not too prohibitive.

Now, given an experimental configuration with perpendicular observation ($\theta_z = 0$) of the scatter within a set volume at a set distance, then many of the parameters in the above equation can be grouped as a single constant

$$\mathbb{C} = \frac{V\pi^2}{\varepsilon_o^2 r^2}\left(\frac{45a^2+7\gamma^2}{45}\right)$$

(37)

which reduces the Rayleigh scattering intensity equation to

$$I_{scatter} = \mathbb{C}\ \frac{I_{laser}}{\lambda^4}\ N\ .$$

(38)

So for a given experimental set up with a constant laser intensity and wavelength we can simply say the Rayleigh scatter intensity is directly proportional to the gas density, or $I_{Scatter} \propto N$.

Now we consider the treatment of the air molecules in the scattering volume as an ideal gas. All of the major constituents of air are relatively small, light, nonpolar molecules, which are characteristics mimicking an ideal gas. At normal ambient conditions such as standard temperature and pressure, air behaves qualitatively like an ideal gas. Therefore, the ideal gas law should apply to the scattering molecules in this analysis, so that

$$P = NkT_{trans}$$

(39)

where, again, N is number density (cm^{-3}), k is the Boltzmann constant and P is the gas pressure. If a constant pressure is assumed within the air scattering sample, then the number density of scattering molecules can be set to

$$N = \frac{P}{kT_{trans}}$$

(40)

and substituting this into the scatter intensity expression gives

$$I_{scatter} = \mathbb{C}\ \frac{I_{laser}P}{\lambda^4 k}\ \frac{1}{T_{trans}}\ .$$

(41)

This expression reveals that the Rayleigh scatter intensity is inversely proportional to the translational temperature of the air sample, or

$$I_{scatter} \propto \frac{1}{T_{trans}}.$$

(42)

This result provides the fundamental relationship which allows laser Rayleigh scattering to be used as a thermometric technique, as was first demonstrated experimentally by Dibble and Hollenbach in 1981 [26].

4   PREVIOUS WORK

4.1   Laser Rayleigh Scattering as a Diagnostic Tool

Rayleigh scattering has been widely used as a diagnostic tool in applications ranging from velocity field measurements, density measurements, characterization of flames and of Earth's atmosphere, gas temperature measurements in flames and more recently gas temperature measurements in plasmas [27]. Dibble and Hollenbach were the first to use Laser Rayleigh Scattering as a gas temperature measurement technique in 1981 [26]. They used the fundamental theoretical result that Rayleigh scattering intensity is inversely proportional to gas temperature for an ideal gas at constant pressure as detailed in the previous section. This relationship allowed them to make spatially resolved gas temperature measurements within turbulent flames at an extremely high acquisition rate with similar accuracy when compared to the thermocouple techniques that were being used at the time. Barat et al. (1991) repeated the technique introduced by Dibble and Hollenbach in a toroidal jet stirred combustor, with the addition of a method of filtering stray light based on polarization of scattered light [28]. Spectrally filtered Rayleigh scattering was used for three dimensional supersonic flow field visualization by Forkey et al. in 1994 [29]. The filtering acted to suppress stray background scatter.

In 1991 Murphy and Farmer examined what temperature regimes Rayleigh scattering may be used for temperature measurement in a thermal plasma. Temperature dependent Rayleigh scattering cross sections for thermal plasmas were calculated. These cross sections were compared with the Thomson scattering cross sections and the plasma regimes in which Rayleigh scattering temperature measurements are possible were examined. It was determined that at low temperatures the Rayleigh scattering process is dominant while at higher temperatures when significant ionization occurs Thomson scattering becomes important. It was also verified in both cases that the incident wavelength is quite important as the wavelength dependence of Rayleigh scattering favors the bluer end of the spectrum. As an example, at approximately 266 nm (as is the case for this work), the plasma temperature must be extremely hot, approaching 10,000 K, for Thompson scattering to account for 1 percent of the scattering signal in a thermal plasma [30]. In 2002 Yalin et al. used filtered Rayleigh scattering for spatially resolved gas temperature measurements in a weakly ionized glow discharge at approximately 50 Torr. The FRS process makes use of a resonant vapor filter, which acts as a narrow band-stop filter at the laser wavelength, in order to suppress stray light as well as some percentage of the total Rayleigh scatter near the filters resonant wavelength. For temperature determination, a model of the temperature and pressure dependent Rayleigh line shape, including the centered depletion from the filter, was fit to experimental results. Additionally, Yalin et al. [31] took advantage of the increased Rayleigh cross section in the ultraviolet and gas temperatures were measured from approximately 350 to nearly 800 K. Also in 2002, Rousseau et al. produced spatially resolved gas temperature measurements derived from absolute Rayleigh scatter intensity for a microwave surface wave discharge (SWD) ranging in power from 20 to 800 Watts and pressures ranging from 2 to 40 Torr. The gas temperatures' dependence upon power density was shown to agree with theoretical predictions using the stationary heat transfer equation.

Additionally, the gas temperatures were seen to be constant along the plasma column, unlike the electron densities [32]. This study also used a low pressure of 2 Torr yet was still able to extract a gas temperature from Rayleigh scattering.

4.2   Microdischarge Characterization

 In the past decade, microdischarge, or microplasma, characterization has seen a great deal of attention. A variety of techniques are used for extraction of plasma parameters. Thomson scattering has been used for electron temperature and electron density measurements, various optical emission spectroscopy techniques for measuring rotational and vibrational temperatures of different species (generally N_2, N_2^+ and OH) as well as techniques for indirectly measuring electron temperature using the radiative-collisional model typically using known emissive argon transitions. Additionally Raman scattering is used to measure rotational and vibrational temperatures of molecules in the microdischarge.

In 2004 Iza and Hopwood used a split wave resonator operating at microwave frequencies to generate an argon/nitrogen microplasma within a 0.120 mm split-ring gap at pressures ranging from 1 to 1000 Torr and power ranging from 0.3 to 1 Watt. They measured electron temperatures from argon lines while vibrational and rotational temperatures were measured for both the second positive and first negative systems of N_2. It was found that the vibrational temperature of N_2^+ derived from the first negative system was significantly higher than that of N_2 derived from the second positive system. The highest rotational temperatures measured by Iza and Hopwood were approximately 400 K [6]. Staack et al. in 2005 performed a thorough characterization of an atmospheric pressure microdischarge ranging from 0.4 to 10 mA with a pin to plate electrode configuration having a separation ranging from 0.05 to 0.5 mm. They performed a current voltage characterization as well as a thorough optical emission spectroscopy study, including rotational and vibrational temperature measurements. From these measurements, and other observations, they concluded that their particular microdischarge could be characterized as a so called normal glow discharge [5]. In the following year, Belostotskiy et al. used rotational Raman scattering to make spatially resolved (approximately 40 μm resolution) rotational temperature measurements in a 500 Torr N_2, 0.3 mm gap microdischarge. Temperatures ranged from approximately 400 to 1200 K depending on radial/axial location [33].

In 2007, Staack et al. imaged the emission from an atmospheric-pressure air microplasma, having an inter-electrode separation of 0.4 mm, directly onto the slit of an imaging spectrometer. David Staack and his colleagues fitted spectra from the second positive system of N_2 and assigned axially resolved rotational and vibrational temperatures. Rotational temperatures throughout the active microdischarge region averaged approximately 1200 K while vibrational temperatures averaged approximately 4500 K. The hottest rotational temperature was measured in the negative glow region of the discharge, peaking at 1450 K, while the lowest temperature was measured within the Faraday dark space at approximately 800 K [9]. Mariotti et al. performed temperature measurements within a 0.3 mm electrode separation microdischarge with an argon and O_2 gas mixture flow. Electron temperatures were deduced from the collisional-radiative model using several argon emission lines while the gas temperature was indirectly measured by fitting the $OH(A^2\Sigma^+, v = 0)$ system. Gas temperatures were measured to range from approximately 900 to 1350 K while electron temperatures ranged between approximately 1 to 2 eV for microdischarge power ranging from 1 to 5 Watts [34].

In another example of a microwave microdischarge characterization, Zhu, Chen and Pu studied a 900 MHz, 60- to 120-μm electrode separation near-atmospheric pressure argon discharge in 2008. Gas temperature measurements were assigned using rotational temperature fits of the $OH(A^2\Sigma^+, v = 0)$ band. Electron density measurements were determined by Stark broadening

of the hydrogen β Balmer line while electron temperature measurements were done using a collisional-radiative model for argon. Values of T_g, n_e, and T_e were measured for ranging electrode separation and discharge power ranging from 0.5 to 2 Watts. Gas temperatures averaged approximately 600 K, electron densities were on the order of $10^{14} cm^{-3}$, while electron temperatures ranged from approximately 1.2 to 1.6 eV [35].

4.3 Comparison and Validation of Techniques within Small Dimension Discharges

As a variety of techniques used to characterize small dimension discharges offer measurements of the same or similar parameters, and these techniques often have similar implementations, attention has been given to comparing and contrasting these methods in the past several years.

In a metal anode to water cathode electrode configuration with a spacing of approximately 3 mm, a comparison was made by Verreycken et al. [37] between OES rotational temperature measurements derived from both the N_2 second positive system and the $OH(A^2\Sigma^+, v = 0)$ band as well as measurements derived from Rayleigh scattering and N_2 rotational Raman scattering. Rayleigh gas temperatures were found to be in good agreement with rotational temperatures derived from the N_2 second positive system (ranging from approximately 2600 to 3200 K) while the $OH(A^2\Sigma^+)$ rotational temperatures were measured to be consistently higher (less dependent upon current and approximately 3600 K) for discharge currents ranging from 15 to 50 mA [36].

In a 2012 publication by van der Gessel et al. [38]; electron temperatures, electron densities, gas temperatures and rotational temperatures of an atmospheric plasma jet with dimensions on the order of several millimeters were measured with 50 µm resolution using a combination of Thomson, Raman and Rayleigh scattering. For the Raman and Thomson scattering measurements, a triple grating spectrometer with a mask was used to filter out the elastic Rayleigh scatter and scattered stray light. Then, an algorithm was written to separate and fit the superimposed spectra of both O_2 and N_2 rotational Raman scattering, as well as the Thomson scattering spectra. This work is possible because in the atmospheric pressure regime and at the densities studied (approximately $10^{14} cm^{-3}$) none of these three scattering mechanisms are overly dominate. At a much lower pressure, the Rayleigh and Raman cross sections would vanish while at lower electron densities the Thomson scattering cross section would vanish. Peak gas temperature was measured to be approximately 600 K, while electron temperatures ranged from approximately 2 to 4 eV, peaking at the radial edge of the discharge as electron densities fall off [37].

5   EXPERIMENTAL

5.1   Microdischarge

The microdischarge used in this investigation was operated in open laboratory air at atmospheric pressure. The electrode configuration and dc circuit were designed so that the microdischarge could operate in normal glow mode for these experiments [5]. The motivation for using a discharge in normal glow mode was to create an environment in which temperature measurements could be made within a nonthermal plasma, where the translational, rotational, vibrational and electron temperatures are not in equilibrium. This non-thermal distribution is ideal for microdischarge applications requiring electronically excited species within a relative low temperature gas, but also presents an interesting test platform for investigating novel temperature measurement techniques.

The electrodes for the dc microdischarge were configured as two closely spaced points, with the inter-electrode gap adjustable from 0 to 2,000 µm, via a micrometer stage under the cathode support. The anode was a 25-µm-diameter stainless steel wire encased in a ceramic cylinder while the cathode was a 200-µm-diameter molybdenum rod that tapered down to a 50 µm rounded tip, where the larger cathode was critical for thermal management of the microplasma. This anode and cathode combination was found to have the surface and thermal characteristics to provide reasonable discharge stability without overheating. Stability issues seen in non-optimized electrode configurations include variation in the discharge path and shape with time, the discharge terminating on various locations near the cathode tip, variations in discharge current and even extinguishing of the discharge. Some electrode configurations that were found to be less than optimal due to instabilities included pin-plate configurations, pin-pin configurations in which the cathode pin was unable to withstand heat and electrodes composed of particular materials which were found to create instabilities.

A Glassman high voltage 10kV, 60 mA maximum DC power supply was used in series with a 1 MΩ, 300W load resistor to energize the microdischarge. A circuit diagram of the microdischarge configuration is shown in Figure 5b. The voltage across the electrodes and the voltage drop across the resistor where both measured with a Tektronix high voltage probe with 1000:1 attenuation and a 40 kV maximum voltage. Additionally, a Simpson donut current sensor was used to measure the discharge current. Both the high voltage probe and current sensor were monitored on a LeCroy WaveRunner digital oscilloscope. This microdischarge current could be adjusted over the range of 2 mA to 7 mA by varying the applied voltage across the load resistor and microdischarge. The resistance across the air gap without a discharge was very high and, with an inter-electrode separation of 0.75 mm, approximately 3,500 V was required to cause breakdown, which agreed well with the predicted value of approximately 3,450 V, from section 3.1. After the initial breakdown, the discharge formation caused the gap resistance to decrease significantly and the voltage drop across the electrode gap needed to sustain the microdischarge ranged from 400 to 600 V, while keeping the microdischarge in the normal glow mode.
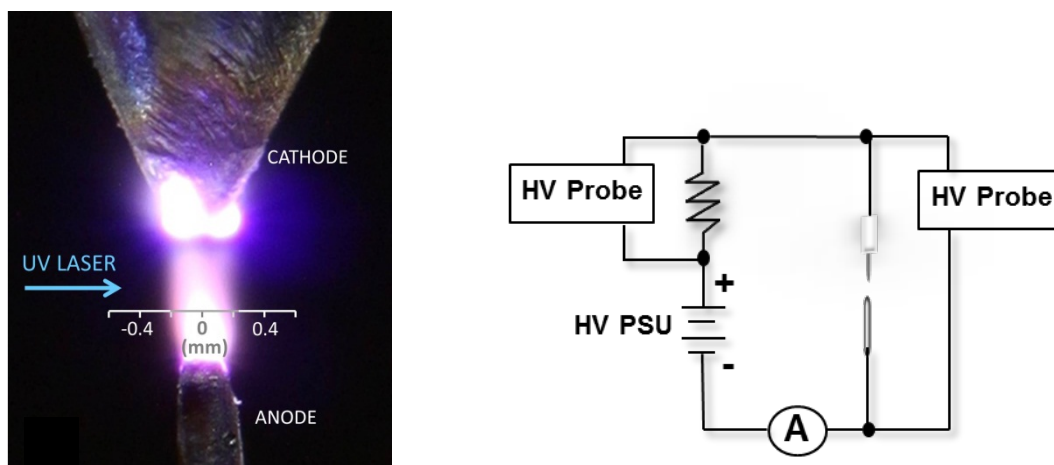
Figure 5: a) Discharge Image Showing Laser Propagation and Relative Scale, and b) Discharge Circuit Design

5.2 Optical Emission Spectroscopy

The continuous OES from the microdischarge was collected through an optical system including a pin-hole for spatial filtering followed by a two lens system of focal lengths 1 cm and 5 cm projecting an enlarged image onto a 1.5 mm diameter fiber optic sensor head as shown in Figure 6 below. Light was collected from a specific microdischarge location by translating the fiber optic sensor head with a spatial resolution of about 300 µm and transmitted by 4m fiber optic cable to the entrance slit of a 0.5 m spectrometer, the Acton pro 500i, with an Andor-DH720 intensified charge-coupled device (ICCD) camera mounted at the CCD port. The spectrometer grating, having 1200 grooves/mm and blazed at 300nm, was centered at 373 nm to isolate the $N_2(C^3\Pi_u \to B^3\Pi_g)$ fluorescence band with $\Delta v = +2$. At this wavelength, the spectrometer and detector had a final resolution of approximately 0.04 nm. Vibrational bands of interest in this region include the $C^3\Pi_u \to B^3\Pi_g$, $v' - v''$ transitions 0-2, 1-3, 2-4 and 3-5. The 0-2 transition with band head at 380.4 nm is the most intense in the region and its rotational structure was the primary feature analyzed in this work. The timing of the spectral acquisition was run by an internal clock separate from that of the Rayleigh acquisition and laser system. The exposure time for each acquisition was ~0.5 ms with a repetition rate of 10 Hz and the high signal-to-noise ratio of the spectrum prevented any need for subtracting background noise.
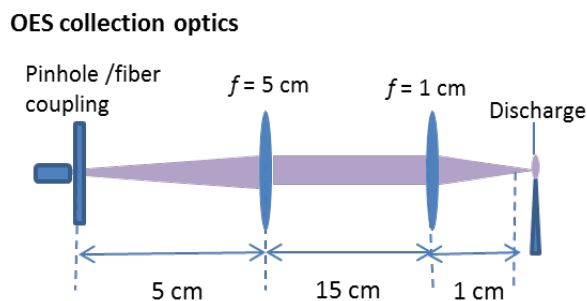

Figure 6: OES Collection Optics

This OES setup enabled spatial filtering and spectral analysis of the central and hottest microdischarge region providing data that was comparable with the laser Rayleigh scatter data. The 300 µm spatial resolution of the emission in a region with significant temperature gradients, though, was much lower resolution than the 20 µm laser scatter image resolution. Also, the light cone of collected emission included some signal from the cooler outer radius of the microdischarge, and thus the rotational temperature analysis represented an average temperature over a larger collection volume compared to the Rayleigh scatter method.

5.3   Rayleigh Scattering Measurements

A sketch of the overall experimental setup is shown in Figure: 9, which includes the OES apparatus, discussed previously, as well as the laser scatter imaging apparatus, which is described in this section. In brief, a pulsed ultraviolet (UV) laser was used to probe the microdischarge and the resulting Rayleigh scattered laser light was collected and imaged.   The ultraviolet laser wavelength of 266 nm (37,590 cm^{-1}) was obtained by frequency quadrupling the output of a Brilliant Nd:YAG laser manufactured by Quantel. This Brilliant laser has a specification output of 330 mJ per pulse at its fundamental 1064 nm, 165 mJ per pulse at 532 nm and 50 mJ per pulse at 266 nm. The ultraviolet laser pulse that passed through the electrodes had a roughly 0.8 cm^{-1} line-width and 7 ns pulse duration, with a nominal energy, after attenuation and beam shaping, of about 8 mJ per pulse. To propagate the laser between the electrodes, the laser beam was focused with a 30 cm focal length quartz lens to produce a beam waist with an approximate full-width at half-maximum (FWHM) of 50 µm with a calculated Rayleigh length of approximately 3 cm. This provided sufficient laser length of relatively uniform radiation and a sufficiently small laser waist for passing between the electrodes. The Rayleigh scatter was collected perpendicular to the laser beam through an adjustable iris and then through two lenses which focused and magnified the Rayleigh scatter image onto an ICCD detector made by Andor. The iris reduced the elastic background component including stray reflections. The image resolution of the scatter intensity along the laser propagation was limited by the pixel density of the ICCD, with an estimated image resolution in that dimension of 20 µm. This resolution was assigned as the spatial uncertainty in the scatter intensity corresponding to temperature profiles along the microdischarge radius. A full diagram of the optical setup of the laser Rayleigh scattering setup is shown in Figure 7. A Stanford Research signal delay generator provided the master clock for the experiment, with the flash-lamps and Q-switch of the Nd:YAG laser and the ICCD camera shutter triggered by delay generator pulses.
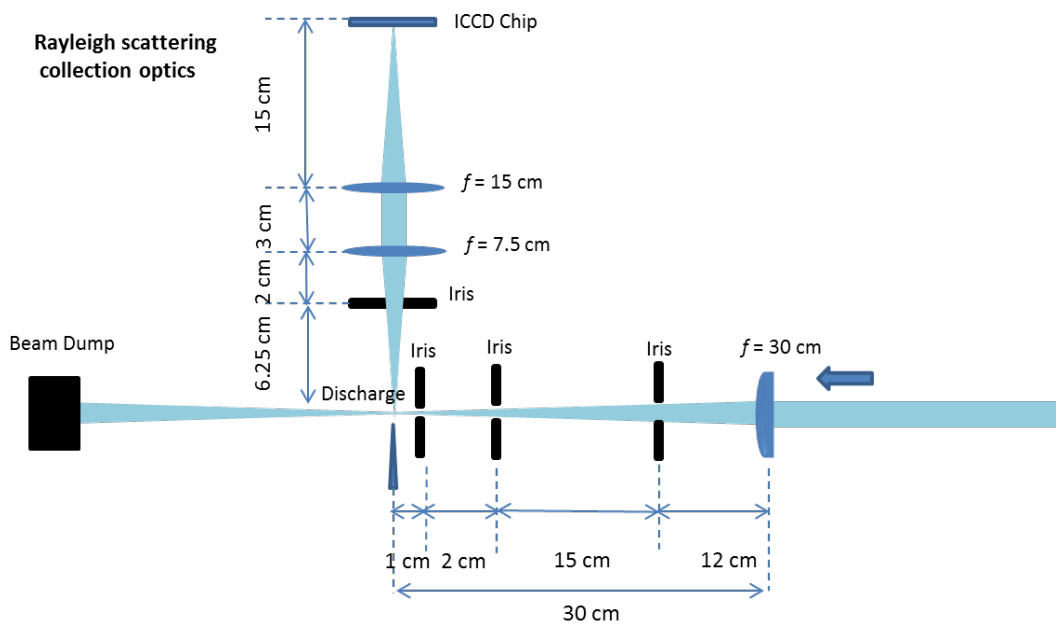
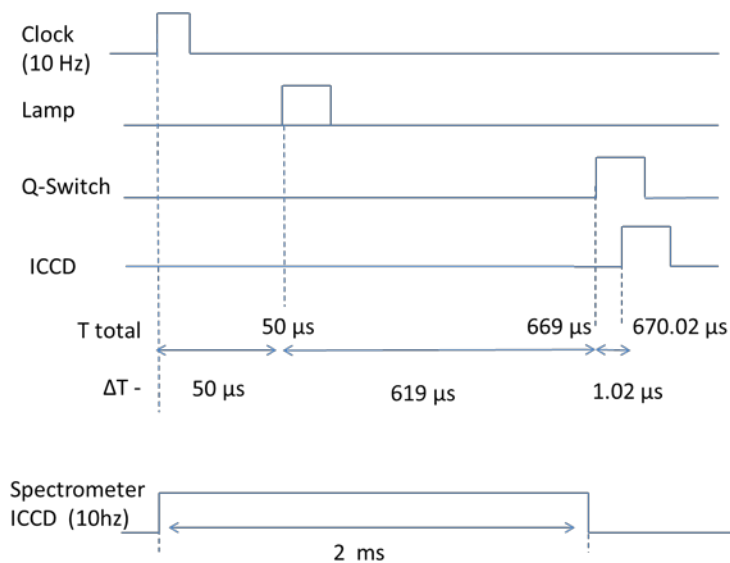**Figure 7: Laser Rayleigh scattering optical setup**

Figure 8: Experiment timing diagram

The ICCD shutter duration was set between 10 and 15 ns, only slightly higher than the 7 ns pulse duration of the laser. This temporal filtering relieved the Rayleigh measurements of most background noise including most of the continuous light emission from the microdischarge.
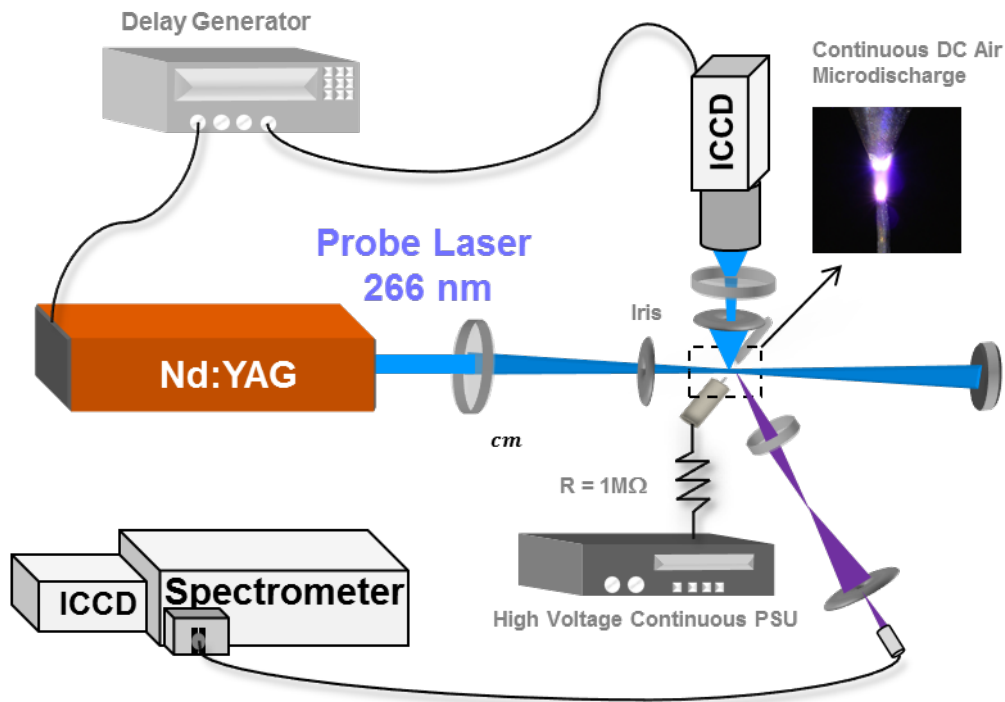
Figure 9: Diagram of experimental setup

5.4 Discharge and Laser Alignment

Because of the small nature of both the microdischarge and the laser beam waist, much care needed to be taken when ensuring the system was properly aligned. In order to be sure that the volume being examined was in fact occupied by the discharge, we needed to be sure that the laser was probing the center of the discharge and that the appropriate laser-discharge interaction region was being imaged onto the ICCD camera. For these reasons, the microdischarge was mounted on a 3 axis micrometer translational stage. Adjustments were made one dimension at a time using a combination of real time ICCD images of the Rayleigh scatter and a second USB microscope camera (Dino-Lite Premier). With the discharge off, the laser and electrodes would be initially aligned by eye, so that the laser propagated through the center of the electrodes, equidistant from each electrode. Then the two cameras, each perpendicular to one axis of the translational stage, were used to fine tune the alignment. The Rayleigh scatter images were used to ensure the laser's position between the electrodes as well as adjust the position of the laser waist, an example of this perspective is shown in Figure10. The second microscopic camera, positioned with a field of view perpendicular to that of the ICCD camera, was used to align the final dimension by observing and minimizing scatter from the electrodes. An example of this second camera's perspective is shown in Figure 11. Further certainty of the alignment could be obtained by recording repeated Rayleigh scatter measurements while translating the energized discharge in one dimension (radially with respect to the discharge's inter-electrode axis) by small steps. Then, by making the assumption that the radial center of the discharge has the highest translational temperature, the Rayleigh scatter measurement which records the least amount of scatter with the discharge on, would be the location closest to the center of the discharge.
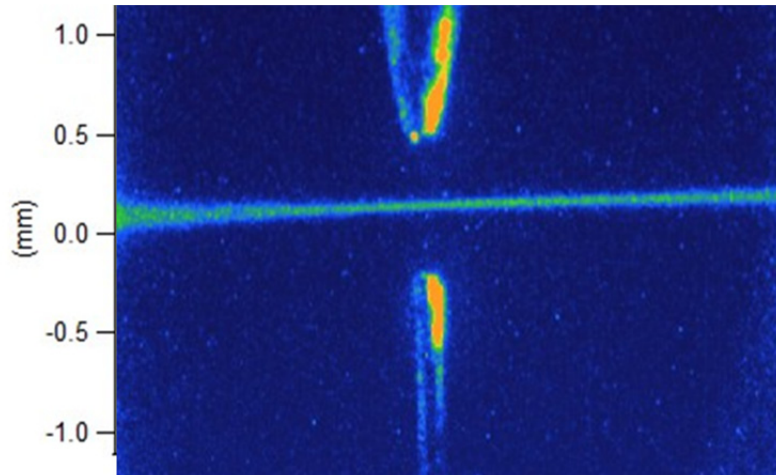
Figure 10: Image of Rayleigh scatter between electrodes.
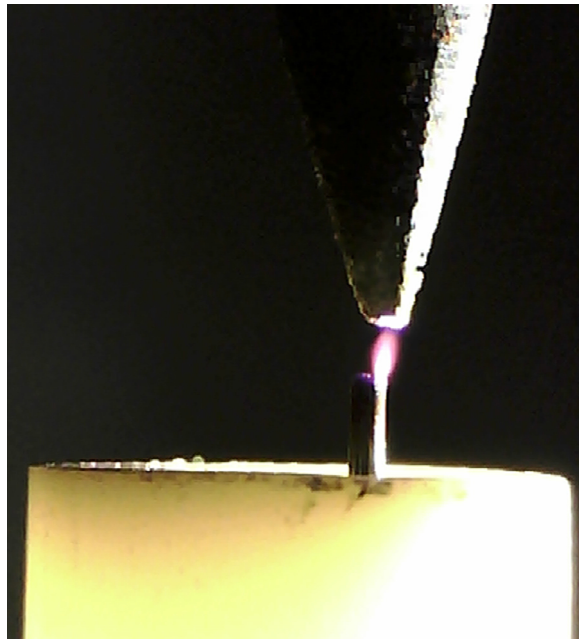
Figure 11: Discharge Image Taken by Microscopic Camera

5.5   Experimental Procedures

The following procedures were adhered to during each data collection. To begin, the Nd:YAG laser was powered on and operated for 1 hour, allowing the laser system and frequency doubling crystals to reach a reasonable degree of thermal equilibrium. This minimized any laser power fluctuations caused by temperature changes in the crystals. The electrode alignment was then double checked to ensure the two electrodes were parallel and shared a line perpendicular to the laser and also had the desired inter-electrode spacing. After ensuring the anode to cathode alignment, the laser was positioned and aligned between the electrodes as described in the

28

section above. Additionally, the electrodes were regularly cleaned using fine sandpaper in order to remove any buildup of films deposited by the discharge. Next, using the image projected by the OES collection optics, the fiber optic sensor head was positioned so that it was nominally equidistant between the electrodes in order to match the probed volume of the laser as closely as possible. Once a nominal optical alignment was achieved for both the OES and Rayleigh apparatus, the discharge was energized with the desired voltage.

For both the scatter imaging and spectral acquisition, it was necessary to integrate or average over multiple accumulated acquisitions to improve signal to noise and eliminate statistical variations. However, the accumulated acquisition of the laser scatter image required more time to complete than that of the emission spectral accumulations. To ensure that the two techniques were observing the discharge over the same time period, the OES spectral accumulations were increased to match the image acquisition time. The two acquisitions were then taken simultaneously. The time to complete one scatter image from within the discharge was ~1 minute for accumulating 100 images, while the OES was accumulating 500 spectra. In an attempt to further account for any temperature variations within the discharge over acquisition times, the discharge was energized and then turned off between acquisitions for the same amount of time for each separate acquisition. While the discharge was off, the baseline Rayleigh scatter through lab air was taken. Taking the baseline or reference image just before the image with the discharge energized minimized any laser power fluctuations.

Once the experiment was aligned and calibrated, and the computer software and ICCD gating was correctly setup, the following procedure was followed for each individual acquisition. First with the discharge off, laser Rayleigh scatter was imaged between the electrodes as a reference. Next the discharge was energized and the HV power supply was tuned for the desired discharge current. Now the OES and laser Rayleigh were taken simultaneously over the same time period as the baseline. Once completed the discharge was powered off for the next reference to be taken.

5.6   Rayleigh Scatter Acquisition and Data Treatment

In addition to Rayleigh scattering, plasma emission, dark or lab noise and scatter from electrodes contributed to the signal collected by the ICCD. To disentangle these contributors, the ICCD chip was divided into two vertically binned horizontal tracks. These tracks, each at different locations on the inter-electrode axis, were chosen so that different contributors to signal could be identified, isolated, and subtracted from the Rayleigh scattering track. Figure 12 illustrates the location of each of these tracks.
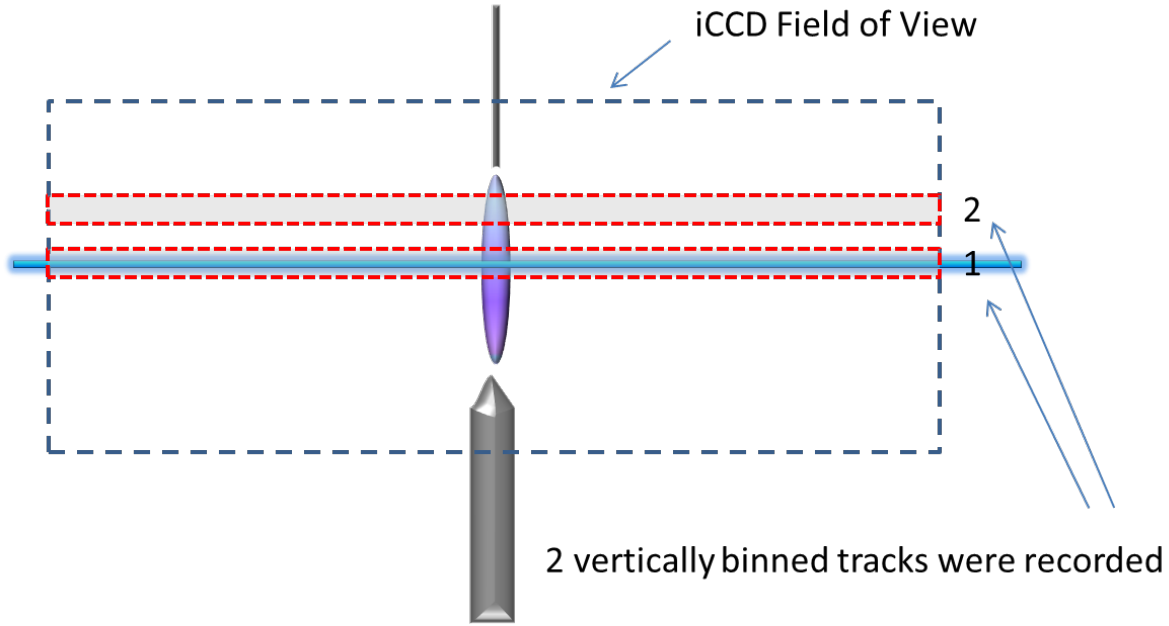
Figure 12: ICCD chip binning configuration

Track 2 contains three out of the four major contributors; plasma emission, nonnegligible amounts of Rayleigh scatter, and dark noise. The major contributor to signal in track 1 is the Rayleigh scatter which we wish to analyze for temperature determination. However, it also contains small amounts of emission from the plasma as well as elastic scatter from the electrodes and dark noise. To complete our analysis we must subtract the contributors so they we are nominally left with only Rayleigh scatter from the plasma, as shown in equation below.

$$I_{Rayleigh} = I_{track1} - I_{dark} - I_{emission} - I_{electrode\ scatter} \qquad (44)$$

$$I_{track\ 2} = I_{Rayleigh(diminished)} + I_{dark} + I_{emission} + I_{electrode\ scatter} \qquad (45)$$

From equation (45), it can be seen that track 2 contains all three elements that need to be subtracted from the primary laser scatter track (track 1), however, track 2 also contains some Rayleigh scatter, although diminished by a factor of ~50, as it is still within the range of the laser. Fortunately, track 2 is located only ~100 µm from track 1 on the inter-electrode axis, thus we can approximate that the gas temperature is the same. Because of this the Rayleigh scatter in track 2 should follow the relative trend of the main Rayleigh scatter in track 1 and subtracting a small fraction of Rayleigh scatter from our main track will have negligable effect on the outcome of the gas temperature. So, by subtracting track 2 from track 1 we are left with the main Rayleigh scatter intensity for temperature determination.

$$I_{Rayleigh} = I_{signal(track\ 1)} - I_{track\ 2} \qquad (46)$$

Now combining this experimentally specific result with our general equation for relative gas temperature as derived in Section 3.5, we have the following equation.

$$T_{gas} = \frac{[I_{track\ 1} - I_{track\ 2}]_{300\ K}}{[I_{track\ 1} - I_{track\ 2}]_{Plasma}} \cdot 300\ K \qquad (47)$$

It can be seen from equation (47) that any diminished Rayleigh scatter from track 2 being subtracted from track 1 will be of little consequence since any scaling reduction in Rayleigh scatter will cancel. The intensities in Equation (47) can be scalar values at an exact location, but for this experiement they were each radially dependent 1-D arrays of detected intensities. The corresponding uncertainty in gas temperature is then given by

$$\sigma_T = T \sqrt{\left(\frac{\sqrt{\sigma_{T\ signal}{}^2 + \sigma_{Back}{}^2}}{I_{T\ Signal} - I_{Back}}\right)^2 + \left(\frac{\sqrt{\sigma_{300K\ signal}{}^2 + \sigma_{Back}{}^2}}{I_{300K\ Signal} - I_{Back}}\right)^2 + \left(\frac{\sigma_{T\ room}}{T_{room}}\right)^2}. \qquad (48)$$

The term $(\sigma_{T\ room}/T_{room})^2$ can be assumed to be negligible compared to our scattering intensity terms. Using the definition that $I_{Rayleigh} = I_{track\ 1} - I_{track\ 2}$, the uncertainty equation becomes

$$\left(\frac{\sigma_T}{T}\right)^2 = \left(\frac{\sigma_{Rayleigh}}{I_{Rayleigh}}\right)^2_{Plasma} + \left(\frac{\sigma_{Rayleigh}}{I_{Rayleigh}}\right)^2_{300K}. \qquad (49)$$

To demonstrate how the uncertainty in the temperature measurement will rise will increasing gas temperature, we can rearrange the equation as follows:

$$\left(\frac{\sigma_T}{T}\right)^2 = \left(\frac{\sigma_{Rayleigh}}{I_{Rayleigh}}\right)^2_{300K} \left(\left(\frac{\sigma_{Rayleigh}}{I_{Rayleigh}}\right)^2_{Plasma} \left(\frac{I_{Rayleigh}}{\sigma_{Rayleigh}}\right)^2_{300K} + 1\right). \qquad (50)$$

Now if we make the assumption that the scatter uncertainty does not change significantly for the 300K or Plasma case, or $\left(\sigma_{Rayleigh}{}^2\right)_{Plasma} = \left(\sigma_{Rayleigh}{}^2\right)_{300K}$, then

$$\left(\frac{\sigma_T}{T}\right)^2 = \left(\frac{\sigma_{Rayleigh}}{I_{Rayleigh}}\right)^2_{300K} \left(\frac{\left(I_{Rayleigh}{}^2\right)_{300K}}{\left(I_{Rayleigh}{}^2\right)_{Plasma}} + 1\right). \qquad (51)$$

From equation (47) we can substitute

$$\frac{T}{300\ K} = \frac{\left[I_{Rayleigh}\right]_{300\ K}}{\left[I_{Rayleigh}\right]_{Plasma}}$$

(52)

and the uncertainty in the temperature measurement becomes

(53)

$$\left(\frac{\sigma_T}{T}\right) = \left(\frac{\sigma_{Rayleigh}}{I_{Rayleigh}}\right)_{300K} \sqrt{\left(\frac{T}{300\ K}\right)^2 + 1}\ .$$

This theoretical equation indicates that the percent uncertainty of the temperature measurement, σ_T/T, is fundamentally dependent on the fractional uncertainty of the Rayleigh scatter intensity $\sigma_{Rayleigh}/I_{Rayleigh}$ at 300K. Due to the temperature analysis technique of calculating the ratio of the reference and plasma Rayleigh intensities, σ_T/T will always be greater than $\left(\sigma_{Rayleigh}/I_{Rayleigh}\right)_{300K}$. For higher temperatures ($T > 1000K$), σ_T/T increases and becomes roughly linear with T. As an example, assuming a reasonable percent uncertainty of 2.5% for the Rayleigh intensity signals, a room temperature plasma would be measured to an accuracy of $T = 300K \pm 11K$, but higher temperature measurements would be $T = 1000K \pm 90K$ and $T = 2000K \pm 340K$. One could conclude from this uncertainty theory that laser Rayleigh scattering temperature measurements for $T < 1000K$ can be fairly accurate, measurements between $1000K$ and $2000K$ would be less accurate but still useful, while measurements for $T > 2000K$ would become so inaccurate that the data may not be useful at all.

6   RESULTS

6.1   Discharge Current-Voltage Characteristics

As an initial study, the current-voltage characteristics of the microdischarge were recorded for electrode spacing ranging from 0.25 to 2.00 mm and power ranging from 0.6 W to 3.1 W. This is an important first step in order to verify the regime of discharge we are working with as well as to define a range of electrode separation and discharge currents for the temperature determination experiments. As atmospheric pressure normal glow discharges are the interest of this work due to their increasing applications and ease of operation, we need to verify that we are indeed in the normal glow regime and not in a neighboring regime such as an abnormal glow or a corona discharge. As discussed in section 3.1, unlike abnormal discharges or coronas, normal glows have a voltage drop that is independent of discharge current for several orders of magnitude, which would manifest itself experimentally as a flat section in an I-V curve.

The results of this initial study in Figure 13 show that the I-V relationship exhibits a relatively flat section, especially for the curves representing smaller electrode spacing. Additionally, at smaller electrode separations, both the current ranges and voltage ranges reflect the common property of a normal glow discussed in the theory section, which is a slight negative differential resistance. For the 0.75 mm case, the discharge voltage ranged from 440 V to 550 V for currents
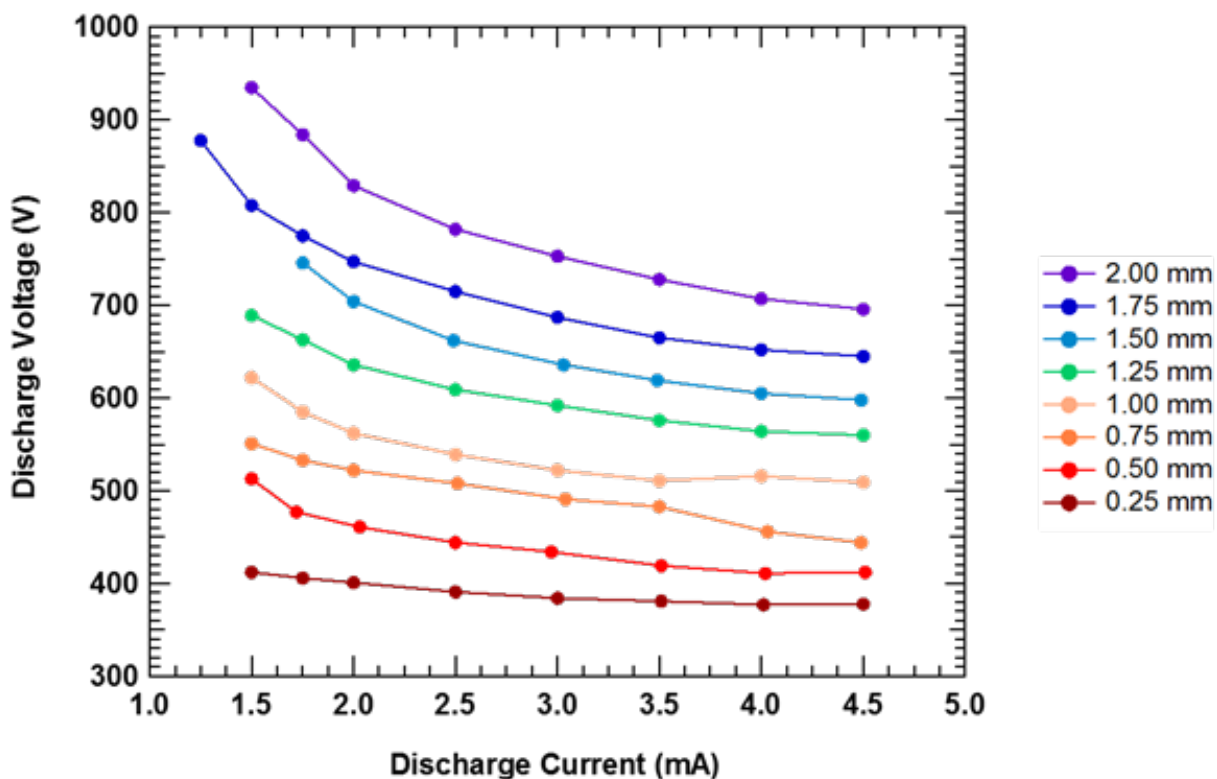

Figure 13: Discharge I-V characteristics for ranging interelectrode separation.

between 1.5 to 4.5 mA.   From this data, the discharge electrical resistance at 3.0 mA can be

calculated to be $R = 180\ k\Omega$, while the differential resistance is $dV/dI = 37\ k\Omega$ at the same current. These values confirm the theoretical stability of this 0.75 mm microdischarge, since the Kaufmann stability criterion states that the resistance, R, must be greater than the absolute value of dV/dI for a stable dc discharge to be sustained [38].

It was desired to work with the smallest electrode separation possible to stay within the normal glow regime. However, due to signal to noise issues from stray light scattering off of electrodes, inter-electrode separations of less than 0.5 mm made Rayleigh scattering measurements increasingly difficult for higher temperatures. Additionally, as it was shown in section 3.2, shorter electrode spacing often leads to less dynamic gas temperatures. For these reasons, an electrode separation of 0.75 mm was chosen for all temperature measurements in this study. This provided adequate inter-electrode space for all optical measurements while also providing a relatively wide range of operating temperatures to investigate temperature measurement diagnostics.

6.2 Rayleigh Scatter Angular Dependence

To experimentally examine the predicted angular dependence of the Rayleigh scatter with the horizontally polarized laser, the laser scatter was collected at both vertical and horizontal orientations from the room temperature air reference condition with the microdischarge off. The scatter signals were sent through the spectrometer, as described in Section 5, so that both the intensity and spectral characteristics could be compared. Figure 6.2 shows the two spectra from a vertically oriented detector ($\theta_z = 0$) on the left and a horizontally oriented ($\theta_z = 90^\circ$) on the right, respectively. The horizontally oriented spectrum has a much lower peak intensity and is displayed with a magnified displayed with a magnified scale of $20 \times$. The calculated ratio of the vertical to horizontal scatter peak signals is $28.1 \times$, which is in close agreement with the theoretical ratio of $29 \times$, derived in Section 3.5. It can be assumed from the theory that the
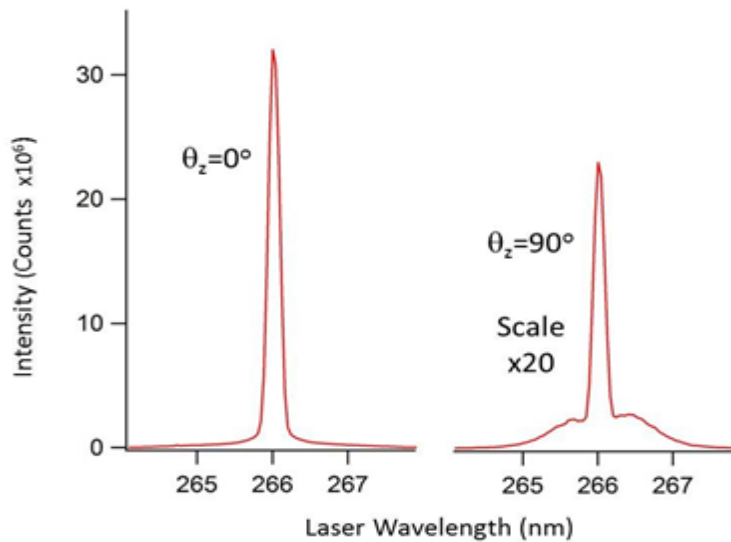

Figure 14: Comparison of Rayleigh scatter observed with $\theta_z = 0$ and $\theta_z = 90^\circ$

spectrum at $\theta_z = 90^\circ$ represents the scatter term that is independent of θ_z and is randomly

polarized, whereas a majority of the scatter at $\theta_z = 0$ is vertically polarized, as the primary term in I_{sV} scatter component. It is also notable that the more intense spectrum at $\theta_z = 0$ is dominated by the un-shifted central wavelength representing elastic Rayleigh scattering, while the weaker $\theta_z = 0$ spectrum reveal "wing" features to the red and blue of the elastic peak that are contours rotational Raman structure. These Raman features were not analyzed further in this work, but do represent an opportunity for measurement of the $N_2(X^1\Sigma_g)$ rotational temperature. These features, though, become much less intense and more disperse under the higher temperature conditions thus requiring high wavelength resolution and generally a means of filtering out the elastic Rayleigh scatter. Similar measurements have been performed by Belostotskiy et al. in 2006 [34] as well as Verreycken et al. in 2011 [37].

6.3 Rayleigh Scattering Temperature Measurements

The following is an example of experimental data collected for a 4.4 mA microdischarge with an inter-electrode spacing of 0.75 mm. Figure 15 shows typical data taken using the experimental methods described in the previous section.
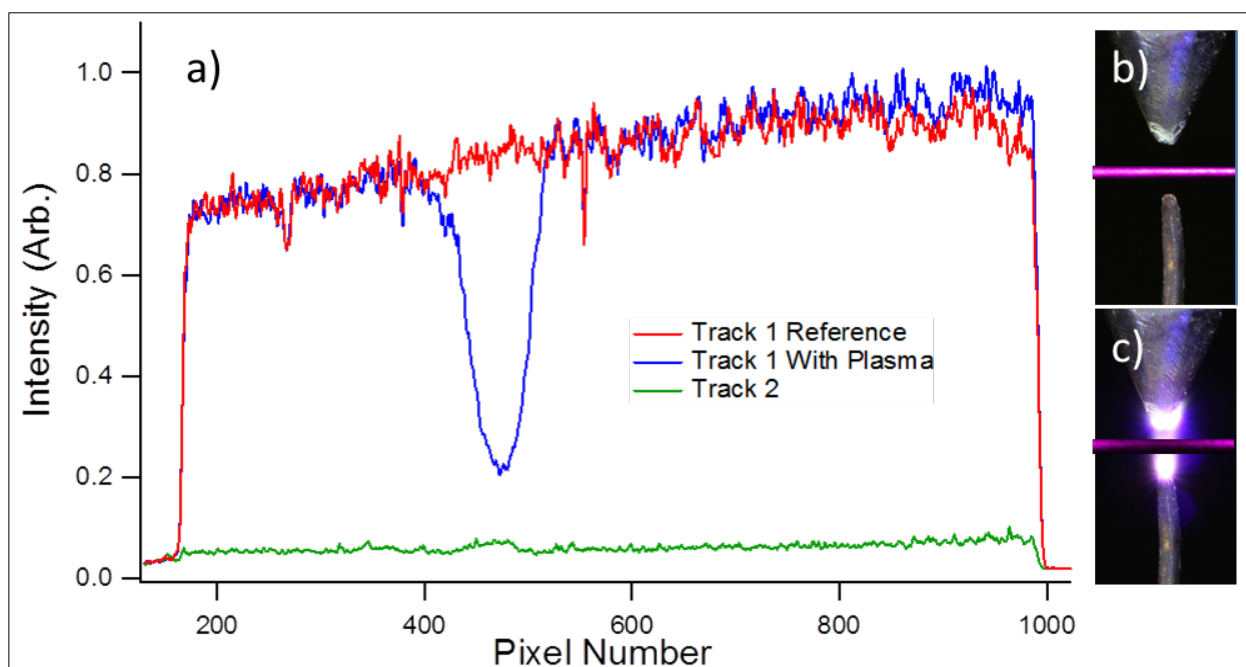

Figure 15: Typical Data from Experimental Methods
((a) Experimental Data for a 4.4mA discharge with an inter-electrode separation of 0.75 mm, b) ICCD Image of Rayleigh scatter superimposed on image of reference condition and represents track 1 reference, and c) ICCD Image of Rayleigh scatter superimposed on image of unknown temperature condition which is track 1 with plasma.)

In Figure 15, each curve represents a vertically binned track collected from the ICCD. Track 1 was taken along the laser while track 2 was taken nominally out of sight of the laser so it may act as a background for subtraction. The reference was taken at room temperature with the plasma discharge off. With the plasma on, the same track shows a near Gaussian decrease in Rayleigh scatter centered at the location of the discharge. Using equation (47), the background (track 2)

was subtracted from both the reference and the scatter through the plasma and their ratio along with the calibration temperature (reference at 300 K) was used to create the radial temperature distribution transversely across the microdischarge shown in the figure below. Figure 16 is the primary result of this work, a high resolution radial gas temperature profile of the microdischarge. It can be seen that the behavior is approximately Gaussian with a peak gas temperature of nearly 1,600 K for a 4.4 mA discharge. Additionally, the gas temperature approaches room temperature approximately 1 mm from the radial center of the discharge. When recording peak temperatures for comparison with OES, the profile was smoothed using a three-point box smoothing algorithm to mitigate noise.
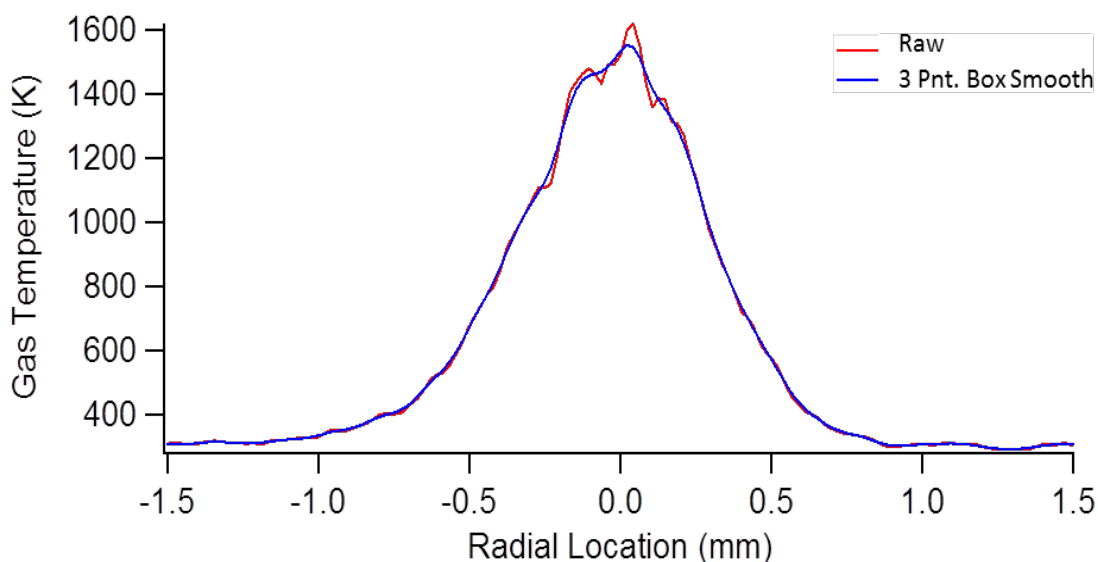

Figure 16: Measured gas temperature distribution for a 4.4 mA, 0.75 mm discharge

Using a procedure identical to the above example radially resolved temperature profiles were extracted for discharge currents ranging from 2.8 mA to 6.0 mA. These measurements were taken equidistant from the electrodes with an inter-electrode separation of 0.75 mm and were nominally at the radial center of the discharge and within the positive column. The image shown in Figure 17 combines radial temperature profiles on the x-axis with current steps of 0.2 mA on the y-axis. The same data is presented as a ribbon plot in Figure 18. It can be seen that the temperature relative width of the discharge increases in an approximately linear fashion with current as does the peak gas temperature. Maximum temperature was observed to be $1,690 \pm 50$ K at a current of 6.0 mA while the minimum temperature measured was 1224 ± 20 K at a current of 6.0 mA. The uncertainties thus ranged from 20 to 50 K and were dependent upon temperature as derived in section 5.6. Additionally, the temperature approaches 300 K between approximately 0.5 and 0.8 mm from the radial center for all discharge currents analyzed.

Approved for public release; distribution unlimited.
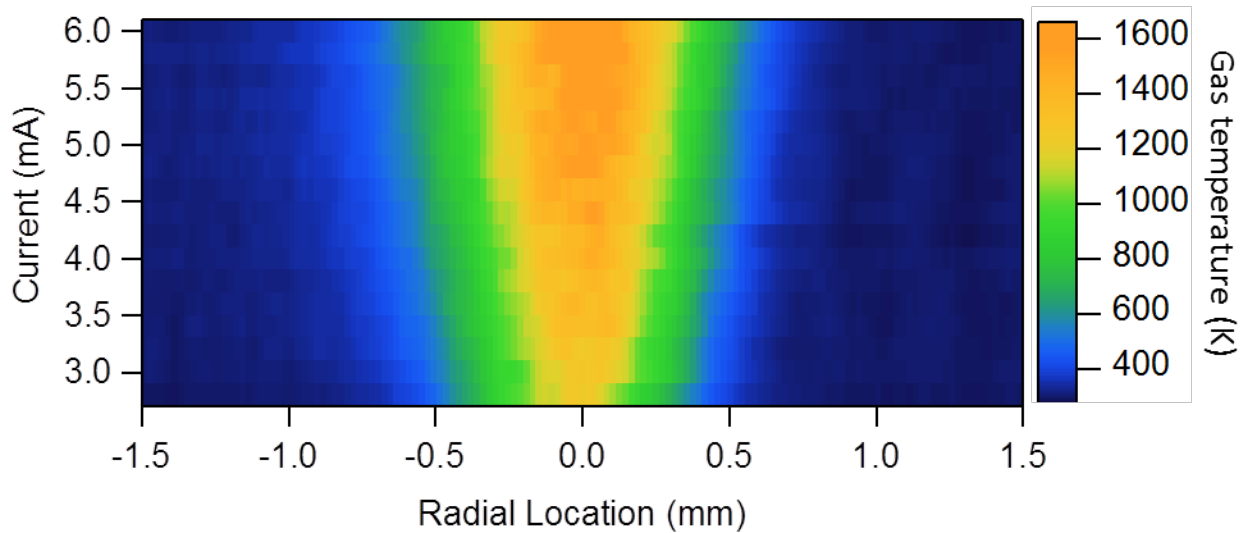
Figure 17: Gas temperature radial distributions measured by laser Rayleigh scattering for currents ranging from 2.8 to 6.0 mA with current resolution of 0.2 mA
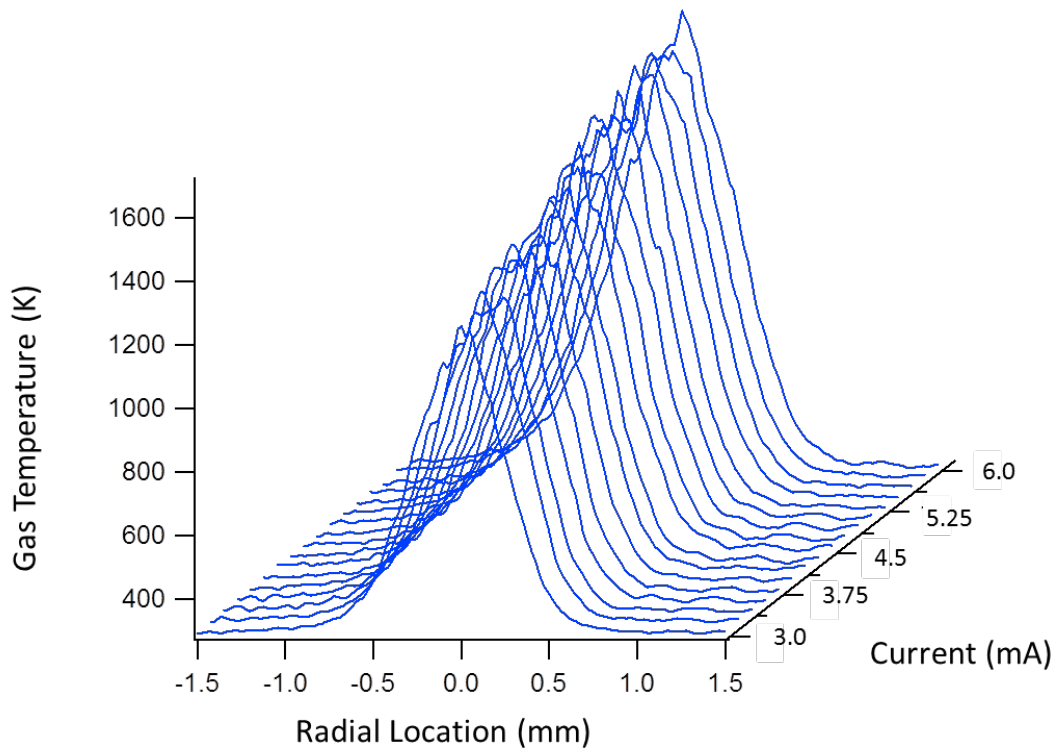
Figure 18: Ribbon plot of gas temperature radial distributions measured by laser Rayleigh scattering for currents ranging from 2.8 to 6.0 mA with current resolution of 0.2 mA

By translating the entire discharge apparatus perpendicular to the laser propagation as well as the inter-electrode axis we were able to resolve the gas temperature in two dimensions, creating a gas temperature slice or a cross-sectional view of the discharge temperature as shown in   Figure

19. We were unable to discern any gravitational dependence with regard to the shape of the discharge temperature distribution as it appears to be radially symmetric for each discharge current considering uncertainties of exact location for each dimension. The vertical dimension is measured by translating the discharge on a micrometer controlled stage while horizontal dimension is measured using ICCD pixels calibrated using images containing the electrodes with known spacing.
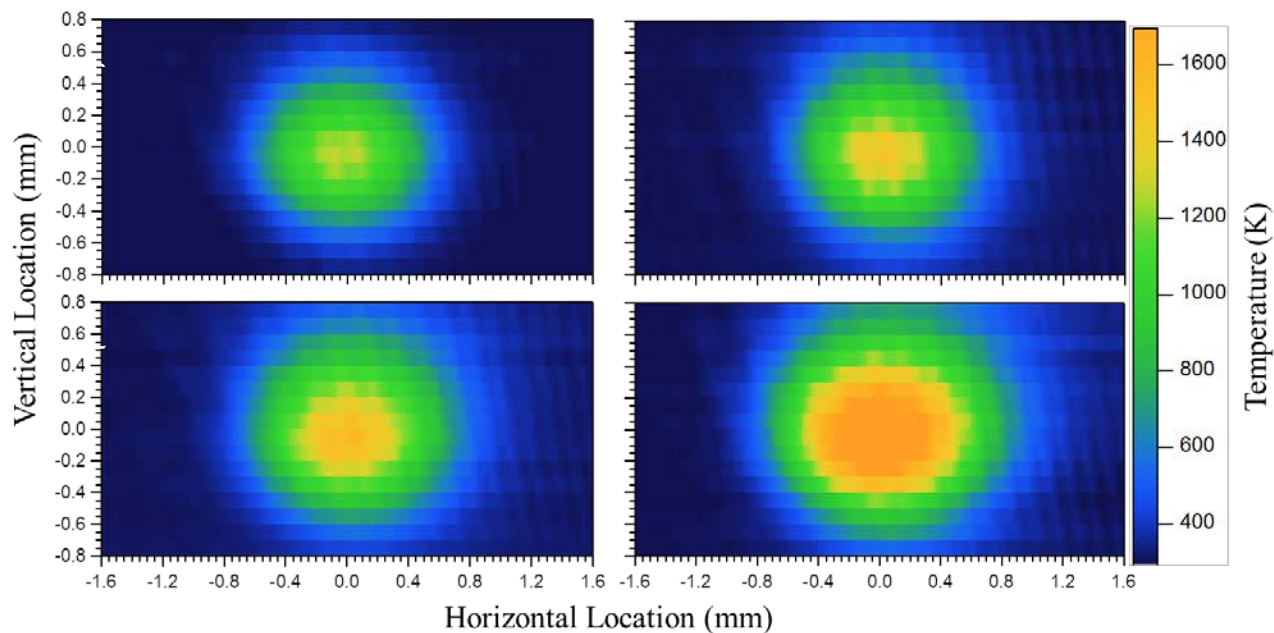
Figure 19: Two-dimensional gas temperature maps measured by Rayleigh scattering for currents of 3-6 mA observed equi-distant from the electrodes

Figure 20 shows the effective gas temperature width of the discharge as measured for currents ranging from 2.8 to 6.0 mA. This data was obtained by fitting the radial temperature distributions to Gaussian functions and extracting the full-width at half maximum (FWHM) parameter. The relationship appears to be nominally linear and the effective temperature width ranges from approximately 180 to 240 µm.

Approved for public release; distribution unlimited.

Figure 20: Effective gas temperature width of discharge measured from Rayleigh scattering radial profiles for currents ranging from 2.8 mA to 6.0 mA

It is expected that some amount of energetic width of the discharge measured here can be attributed to spatial variation of the discharge itself while accumulating scattering data, despite the discharge having appeared to be nominally spatially stable. This may also have 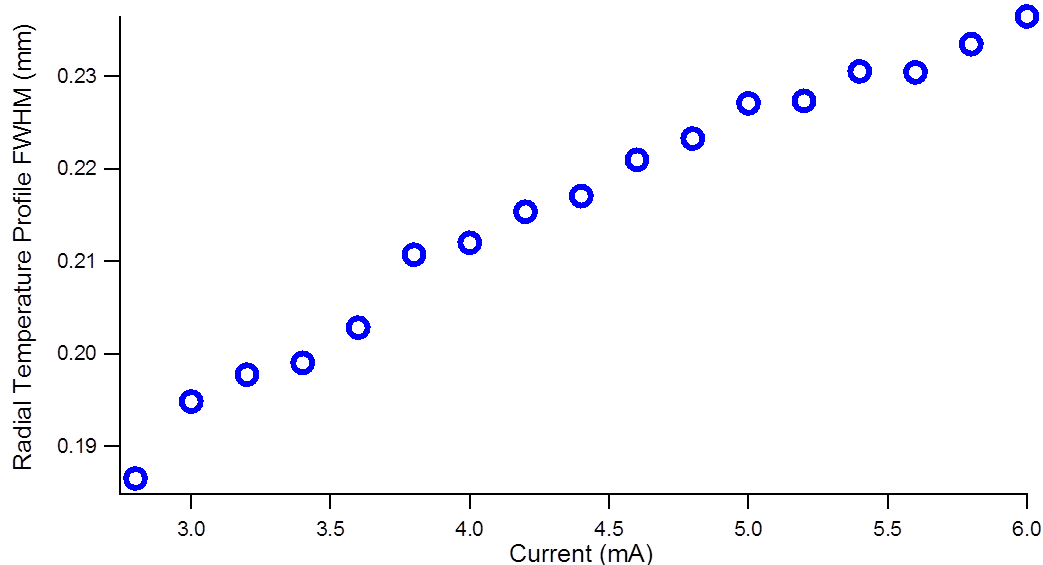acted to decrease the peak temperature of the discharge as for each exposure of the ICCD the hottest point may have been at a slightly different location. As a result, balancing the amount of time integration with the general shot signal-to-noise ratio was important. For this reason time integration was minimized while keeping the signal to noise sufficiently low to provide a reasonable low gas temperature uncertainty.

6.4   Experimental OES Measurements

Optical emission from the microdischarge was recorded and analyzed for microdischarge currents ranging from 2 to 6mA. The $N_2(C^3\Pi_u)$ rotational temperatures, which should correlate to the $N_2(X^1\Sigma_g^+, v = 0)$ rotational temperatures, were derived from fitting $v' - v'' = (0 - 2)$ bands of the N_2 second positive system. An ICCD image of the microdischarge, taken through a band-pass filter centered at 350 nm is shown in Figure 21. This image shows the spatial distribution of the discharge emission, and primarily represents the SPS (second positive system) emission necessary for measuring the rotational temperature. As shown, the majority of emission originates from the plasma sheaths adjacent to each electrode. However, the volume of discharge probed by Rayleigh scattering at the axial center exhibits highly diminished emission and becomes immeasurable at >0.1 mm from the radial center. Even so, the resulting emission spectra at the axial and radial center, was more than sufficient with respect to signal to noise. The spatial resolution of the OES collection apparatus as discussed in the previous section was ~20-30μm and allowed the observed volume of the discharge (as shown by the circle and cross-hair in Figure 21) to nominally match the Rayleigh scattering probe volume.
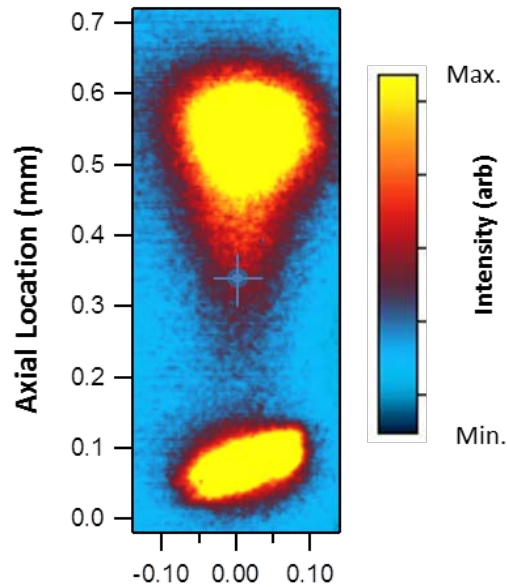
Figure 21: Image of discharge emission through a band-pass filter centered at 350 nm
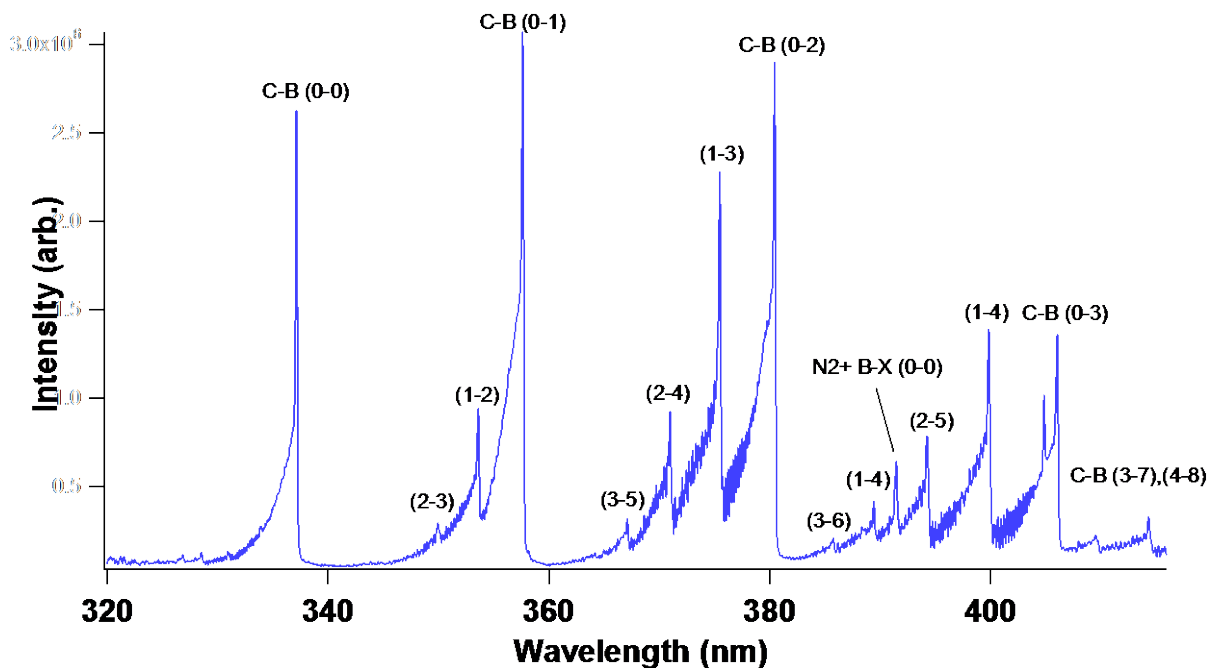
Figure 22: Experimental spectra taken from center of the microdischarge, includes emission from the SPS and FNS

Figure 22 shows an experimental spectrum observed from the location indicated by the crosshairs in Figure 21 from 320 to 415 nm. This region contains four band groups from the second positive system as well as the spectrum from the first negative system $N_2^+ (B \rightarrow X)$ [23].

The model developed by our group is capable of generating simulated spectra for this entire region of N_2 spectra; however, it is preferable to isolate one of the systems at a time for analysis. All of the $N_2(C^3\Pi_u \rightarrow B^3\Pi_g)$ systems accessible were investigated for their potential in determining rotational temperatures, including the $v' - v'' = (0 - 3), (0 - 2), (0 - 1), (0 - 0)$ systems. For this experiment, the $v' - v'' = (0 - 2)$ system centered at ~373 nm was chosen for rotational temperature analysis because of its high intensity, well resolved rotational structure and its common use in this type of analysis [20].

Figure 23: Experimental data for the $(C - B), v' - v'' = (0 - 2)$ band system fit to simulated spectra, with absolute error

Approved for public release; distribution unlimited.

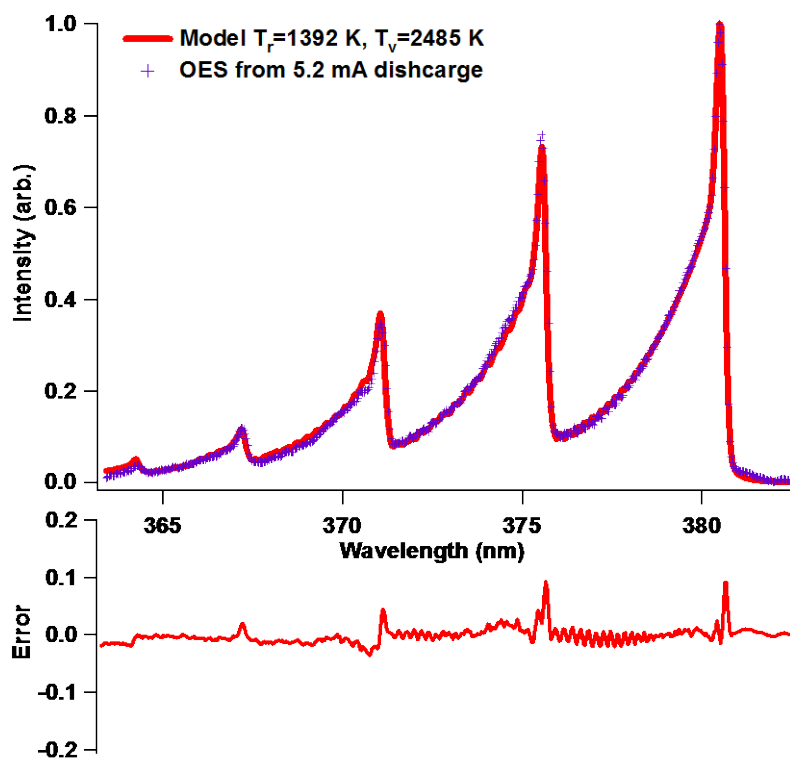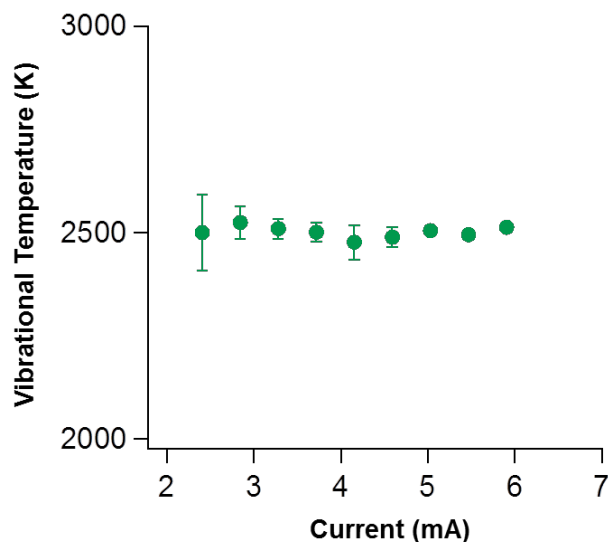**Figure 24: Vibrational temperature from $N_2(C - B)$, $v' \text{-} v'' = (0 - 2)$ system**

The experimental spectrum, shown above, was collected using our primary OES collection setup, as discussed in Section 5, and showed good agreement with the simulated spectrum assuming a Boltzmann energy distribution. Rotational temperatures ranged from 1250 K to 1710 K for currents from 2.8 to 6.0 mA; however, vibrational temperatures were not dynamic and were approximately 2,500 K for all discharge currents as show in Figure 24.

6.5 Comparison of Rayleigh Gas Temperatures with OES Rotational Temperatures

Results comparing rotational temperatures, determined by OES, and the peak translational temperatures, determined by Rayleigh scatter, for various microdischarge currents are shown in Figure 25: Comparison of peak gas temperature measured from laser Rayleigh scattering to radially centered rotational temperature as measured by OES of the SPS It was found that for each measured value, the temperatures were in agreement within experimental uncertainties. This result is consistent with the common assumption made when making temperature measurments using OES methods; that by measuring the excited $N_2(C^3\Pi_u)$ state's rotational temperature, you may estimate the gas temperature to have the same value. As discussed in section 3.3, the $N_2(C^3\Pi_u)$ states rotational energy distribution is representative of that of the $N_2(X^1\Sigma_g^+)$ state because of the direct mapping involved in the excitation/relaxation process. Additionally, it is a common assumption that for these atmospheric air microdischarges the rotational temperature is in equilibrium with the gas or translational temperature. Thus a measurement of the $N_2(C^3\Pi_u)$ rotational temperature is an indirect measurement of the translational temperature. The results of this experiment verify these assumptions as well as provide evidence of the utility of this Rayleigh scattering method for determination of high spatial resolution translation and rotational temperatures in atmospheric discharges.
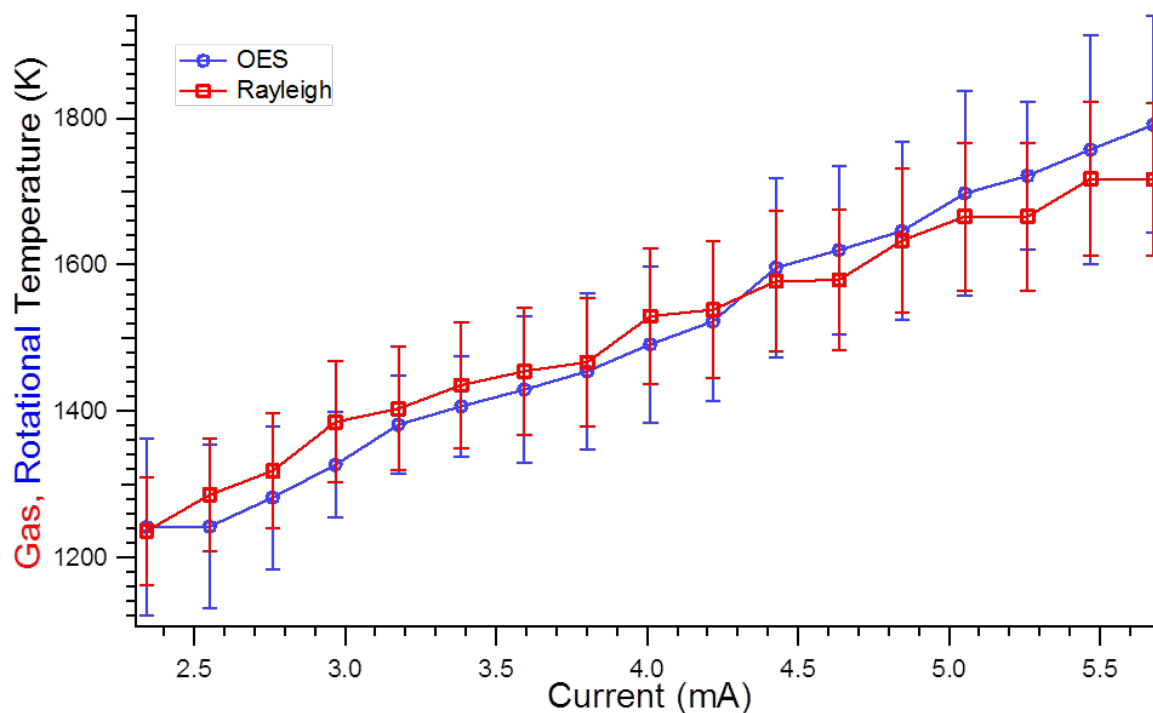
Figure 25: Comparison of peak gas temperature measured from laser Rayleigh scattering to radially centered rotational temperature as measured by OES of the SPS

6.6   Results of Additional OES Investigation Attempts

An ideal comparison of the OES and Rayleigh scattering methods would compare the two temperature measurements at different spatial locations within the microdischarge. Because each Rayleigh scattering measurement was a radial temperature distribution, attempts were made to analyze the optical emission at the same locations with similar resolution. With an experimental setup similar to Staack et al. (2007), the discharge emission was magnified and imaged onto the slit of our 0.5-m spectrometer such that each horizontal row of ICCD pixels contained emission spectra from a different radial location. However, this was made difficult by the fact that the region being analyzed, within the positive column, was only approximately 200 µm in width (approximately equal to the FWHM of Rayleigh radial temperature distributions). Additionally, stray light from the highly emissive negative glow overwhelmed any light collected away from the radial center of the positive column. Thus, radially resolving the rotational temperature via OES was not possible with the configuration used due to low signal-to-noise. The technique was limited to the radially centered location analyzed (approximately 20-30 µm wide) in sections 6.2-3.

7   CONCLUSIONS

7.1   Summary of Results and Conclusions

High resolution radially resolved gas temperature profiles were measured using ultraviolet Rayleigh scatter imaging in an atmospheric air microdischarge plasma. Peak gas temperatures ranged from 1,224 to 1,690 K with a maximum uncertainty of ±50 K while the overall gas temperature profiles exhibited near Gaussian behavior. By translating the microdischarge apparatus vertically with respect to the laser, two dimensional gas temperature maps were generated from within the positive column of the discharge with a resolution of 20 µm. Measured gas temperatures were shown to agree with rotational temperatures measured from the N_2 second positive system.

One key difference between the two measurement techniques examined in this work is the spatial regions within the discharge in which each technique is effective. The Rayleigh scattering method can probe any radial location up to a temperature of approximately 2,000 K and is limited to near the axial center for small electrode spacing due to stray light scattering off of the electrodes. Even so, the laser Rayleigh technique is able to probe discharge dark spaces which are off limits to even highly efficient OES setups. Optical emission spectroscopy however, proved very challenging in providing radial resolution of temperature, but was able to provide accurate gas temperatures with limited axial resolution within the positive column and negative glow.

Using the Rayleigh scattering experimental setup described in Section 5.3, gas temperature measurements from within the discharge were possible at any location up to approximately 250 µm away from either electrode. With greater care in removing stray light or the addition of high spectral resolution filtering it is deemed possible to make measurements in smaller discharges and thus closer to the electrodes using a similar laser Rayleigh scatter experimental setup.

7.2   Future Work

This work has opened up numerous opportunities for further investigation. A natural extension of this work would be to include additional characterizations, such as electron temperature and electron density measurements using Thomson scattering or a collisional-radiative model as well as a more thorough OES study which includes rotational temperature measurements from NO and N_2^+. Another continuation of this work would be to more accurately model expected gas temperatures using the stationary heat transfer equation and to make comparisons to experimentally measured radial and axial gas temperature profiles.

Using high spectral filtering, for example with a triple grating spectrometer, it may be possible to drastically reduce stray light and increase signal to noise in Rayleigh scattering temperature measurements by filtering out the peak wavelength and examining the wavelength shifted scattering only. This may not only reduce the uncertainty but make it possible to measure gas temperatures in close proximity to electrodes and in much smaller microdischarges.

Approved for public release; distribution unlimited.

8   REFERENCES

[1]   K.H. Becker, K.H. Schoenbach and J.G. Eden, "Microplasmas and Applications," *J. Phys. D: Appl. Phys.,* pp. R55-R70, 2006.

[2]   A. Schutze, J.Y. Jeong, S.E. Babayan, J. Park, G.S. Selwyn and R.F. Hicks, "The Atmospheric-Pressure Plasma Jet: A Review and Comparison to Other Plasma Sources," *IEEE Transactions on Plasma Science,* Vol. 26, No. 6, pp. 1685-1694, 1998.

[3]   Y. Akishev, M. Grushin, V. Karalnik, A. Petryakov, and N. Trushkin, "Non-Equilibrium Constricted DC Glow Discharge in N_2 Flow at Atmospheric Pressure: Stable and Unstable Regimes," *J. Phys. D: Appl. Phys.,* p. 075202, 2010.

[4]   N.R.C. Plasma Science Committee, "Plasma Science: Advancing Knowledge in the National Interest," The National Academies Press, 2007.

[5]   D. Staack, B. Farouk, A. Gutsol and A. Fridman, "Characterization of a DC Atmospheric Pressure Normal Glow Discharge," *Plasma Sources Sci. Technol.,* pp. 700-711, 2005.

[6]   F. Iza and J.A. Hopwood, "Rotational, Vibrational, and Excitation Temperature of a Microwave-Frequency Microplasma," *IEEE Transactions on Plasma Science,* Vol. 32, No. 2, pp. 498-504, 2004.

[7]   G.P. Davis and R.A. Gottscho, "Measurement of Spatially Resolved Gas-Phase Plasma Temperatures by Optical Emission and Laser-Induced Fluorescence Spectroscopy," *Journal of Applied Physics,* Vol. 54, p. 2080, 1983.

[8]   Y.C. Hong and H.S. Uhm, "Microplasma Jet At Atmospheric Pressure" *Applied Physics Letters,* Vol. 89, No. 22, p. 221504, 2006.

[9]   D. Staack, B. Farouk, A.F. Gustol and A. Fridman, "Spatially Resolved Temperature Measurements of Atmospheric-Pressure Normal Glow Microplasmas in Air," *IEEE Transactions on Plasma Science,* Vol. 35, No. 5, pp. 1448-1455 , 2007.

[10] C.O. Laux, T.G. Spence, C.H. Kruger and R.N. Zare, "Optical Diagnostics of Atmospheric Pressure Air Plasmas," *Plasma Sources Sci. Technol.,* pp. 125-138, 2003.

[11] A.N. Goyette, J.R. Peck, Y. Matsuda, L.W. Anderson and J.E. Lawler, "Experimental Comparison of Rotational and Gas Kinetic Temperatures In N_2 and *He-N_2* Discharges"*Journal of Physics D: Applied Physics,* Vol. 31, No. 13, p. 1556, 1998.

[12] E. Nasser, Fundamentals of gaseous ionization and plasma electronics, New York: Wiley-Interscience, 1971.

[13] R.B. Miles, W.R. Lempert and J.N. Forkey, "Laser Rayleigh Scattering," *Measurement Science and Technology,* Vol. 12, pp. R33-R51, 2001.

[14] N. Britun, M. Gaillard, A. Ricard, Y.M. Kim, K.S. Kim and J.G. Han, *Journal of Physics D: Applied Physics,* Vol. 40, p. 1022, 2007.

[15] E.E. Kunhardt, "Generation of Large-Volume, Atmospheric-Pressure, Nonequilibrium Plasmas," *IEEE Transactions on Plasma Science,* Vol. 28, No. 1, pp. 189-200, 2000.

[16] I. Langmuir, "Oscillations in Ionized Gases," *Physics,* p. 627, 1928.

[17] D.B. Go and D.A. Pohlman, "A Mathematical Model of The Modified Paschen's Curve For Breakdown in Microscale Gaps," *Journal of Applied Physics,* vol. 107, p. 103303, 2010.

[18] R. Warren, "Interpretation of Field Measurements in the Cathode Region of Glow Discharges," *Physical Review,* Vol. 93, No. 6, pp. 1658-1662, 1955.

[19] Y.P. Raizer, Gas Discharge Physics, Springer, 1991.

[20] D. Staack, B. Farouk, A.F. Gustol and A.A. Fridman, "Spectroscopic Studies and Rotational and Vibratinoal Temperature Measurements of Atmospheric Pressure Normal Glow Plasma Discharges in Air," *Plasma Sources Sci. Technol.,* Vol. 15, pp. 818-827, 2006.

[21] G. Herzberg, Molecular Spectra and Molecular Structure: Spectra of Diatomic Molecules, 1989.

[22] H. Shimizu, K. Noguchi and C.-Y. She, "Atmospheric Temperature Measurement by High Spectral Resolution Lidar," *Applied Optics,* Vol. 25, No. 9, pp. 1460-1466, 1986.

[23] A. Lofthus and P.H. Krupenie, "The Spectrum of Molecular Nitrogen," *J. Phys. Chem. Ref. Data,* Vol.6, No. 1, pp. 113-307, 1977.

[24] F.R. Gilmore and R.R. Laher, "Franck-Condon Factors, R-Centroids, Electronic Transition Moments, and Einstein Coefficients for Many Nitrogen and Oxygen Band Systems," Defense Nuclear Agency, Alexandria, VA, 1992.

[25] J.D. Jackson, Classical Electrodynamics 3rd ed., John Wiley & Sons, Inc. , 1999.

[26] D.A. Long, Raman Spectroscopy, New York: McGraw-Hill, 1977.

[27] R.W. Dibble and R.E. Hollenbach, "Laser Rayleigh Thermometry in Turbulent Flames," in *Symposium on Combustion*, The Combustion Institute, 1981.

[28] R.B. Miles, W.R. Lempert and J.N. Forkey, *Meas. Sci. Technol.,* Vol. 12, No. 5, pp. R33-R51, 2001.

[29] R.B. Bara, J.P. Longwell, A.F. Sarofim, S.P. Smith and E. Bar-Ziv, "Laser Rayleigh scattering for flame thermometry in a toroidal jet stirred combustor," *Applied Optics,* Vol. 30, No. 21, pp. 3003-3010, 1991.

[30] J.N. Forkey, W.R. Lempert, S.M. Bogdonoff and R.B. Miles, "Volumetric Imaging of Supersonic Boundary Layers Using Filtered Rayleigh Scattering Background Suppression," in *2nd Aerospace Sciences Meeting & Exhibit*, Reno, NV, 1994.

[31] A.B. Murphy and A.J.D. Farmer, "Temperature Measurement in Thermal Plasmas By Rayleigh Scattering," *J. Phys. D: Appl. Phys.,* pp. 634-643, 1992.

[32] A.P. Yalin, Y.Z. Ionikh and R.B. Miles, "Gas Temperature Measurements in Weakly Ionized Glow Discharges with Filtered Rayleigh Scattering," *Applied Optics,* Vol 41, No 18, pp. 3753-3762, 2002.

[33] A. Rousseau, E. Teboul, M.J. v d Sande and J.A.M. v d Mullen, "Spatially Resolved Gas Temperature Measurements by Rayleigh Scattering in a Microwave Discharge," *Plasma Sources Sci. Technol.,* pp. 47-52, 2002.

[34] S.G. Belostotskiy, Q. Wang, V.M. Donnelly and D.J. Economou, "Three-Dimensional Gas Temperature Measurements in Atmospheric Pressure Microdischarges Using Raman Scattering," *Applied Physics Letters,* p. 251503, 2006.

[35] D. Mariotti, Y. Shimizu, T. Sasaki and N. Koshizaki, "Gas Temperature and Electron Temperature Measurements by Emission Spectroscopy For an Atmospheric Microplasma," *J. Appl. Phys.,* p. 013307, 2007.

[36] X.-M. Zhu, W.-c. Chen and Y.-K. Pu, "Gas Temperature, Electron Desnity and Electron Temperature Measurement in a Microwave Excited Microplasma," *J. Phys. D: Appl. Phys.,* p. 105212, 2008.

[37] T. Verreycken, A.F.H. v. Gessel, A. Pageau and P. Bruggeman, "Validation of Gas Temperature Measurements by OES in an Atmospheric Air Glow Discharge With Water Elecrodes Using Rayleigh Scattering," *Plasma Sources Sci. Technol.,* p. 024002, 2011.

[38] A.F.H. van Gessel, E. A.D. Carbone, P.J. Bruggeman and J.J.A.M. van der Mullen, "Laser Scattering on an Atmospheric Pressure Plasma Jet: Disentangling Rayleigh, Raman and Thomson Scattering," *Plasma Sources Sci. Technol.,* p. 015003, 2012.

LIST OF SYMBOLS, ABBREVIATIONS, AND ACRONYMS

ACRONYM   **DESCRIPTION**

A	ionization coefficient
B	ionization coefficient
$\mathbb{C}$	consolidation of experimentally constant values
c	speed of light
D	electrode separation
E	energy
E_{li}	laser electric field with polarization, i
E_s	scattered electric field
E_{sH}	scattered electric field, horizontally polarized
E_{sV}	scattered electric field, vertically polarized
F_v	rotational energy term at vibrational level v
G	vibrational energy term
$\hat{H}$	horizontal unit vector
h_{axial}	heat diffusion coefficient for radial cooling
h_{radial}	heat diffusion coefficient for radial cooling
I	electric current
I_{laser}	laser intensity
$I_{n'v'J' \rightarrow n''v''J''}$	light intensity from transition
I_{sH}	scattered intensity, horizontally polarized
I_{sV}	scatter intensity, vertically polarized
J	rotational quantum number
j	current density
k	gas/electrode conductivity
k_b	Boltzmann Constant
N	number density
P	pressure
q	Franck Condon Factor
q_{radial}	heat loss rate due to radial cooling
R	radius
r	distance from particle
$\boldsymbol{R_e}$	electronic transition moment
R_∞	effective radius where $\Delta T = 0$
S	Honl-London Factor
T_e	electron temperature
T_{rot}	rotational temperature
T_{trans}	translational temperature
T_{vib}	vibrational temperature
V	volume
v	vibrational quantum number
$\hat{V}$	vertical unit vector
V_b	breakdown voltage

V_n	gap voltage
α_{ij}	polarizability tensor
γ	anisotropy
γ_i	secondary electron emission coefficient
ε_0	vacuum permittivity
ΔT	temperature differential
θ_z	angle made with polarization of the laser
λ	wavelength
p	dipole moment
$\vec{p}$	polarization vector
φ	angle made with incident light propagation vector
ψ_{el}	electron wave function
ψ_{vib}	vibrational wave function
ψ_{rot}	rotational wave function
$\Psi_{molecule}$	molecular wave function
ω_p	plasma power